

Properties of fast and slow endogenous buffers at the presynaptic terminals of the crayfish neuromuscular junction

Victor Matveev

Department of Mathematical Sciences,
New Jersey Institute of Technology
Tel. 973-596-5619, email: matveev@njit.edu

Jen-Wei Lin

Department of Biology
Boston University
Tel. 617-353-3443, email: jenwelin@bu.edu

CAMS Report 0506-12, Fall 2005/Spring 2006
Center for Applied Mathematics and Statistics

February 11, 2006

Properties of fast and slow endogenous buffers at the presynaptic terminals of the crayfish neuromuscular junction

Victor Matveev [†], Jen-Wei Lin [#]

[†] Department of Mathematical Sciences, New Jersey Institute of Technology,
Newark, New Jersey 07102

[#] Department of Biology, Boston University, Boston, Massachusetts 02215

Correspondence: Victor Matveev, Dept of Mathematical Sciences, NJIT,
University Heights, Newark, NJ 07102-1982. Tel.: 973-596-5619, fax: 973-596-
5591, e-mail: matveev@njit.edu

Running title: Endogenous Ca²⁺ buffers in crayfish NMJ

Keywords: calcium diffusion, calcium buffer, buffering capacity, binding ratio,
computer model, exocytosis, presynaptic mechanisms

ABSTRACT

Endogenous Ca^{2+} buffers (ECBs) typically bind 98% to 99.9% of cytosolic Ca^{2+} , and therefore play an important role in regulating synaptic transmission and other Ca^{2+} -dependent processes; however, the biophysical characteristics of buffers are unknown in most cell types. We attempt to infer the kinetic properties of ECBs at the crayfish inhibitor neuromuscular junction, exploring the recent suggestion by Lin et al. (2005) that an endogenous buffering system consisting of one fast and one slow buffer can account for the time course of Ca^{2+} transients recorded in this preparation. It was proposed that the ECB with slow Ca^{2+} binding-unbinding kinetics controls the decay time course of the AP-evoked Ca^{2+} transient ($\tau_{\text{decay}} \sim 50$ ms), whereas the fast buffer reduces the amplitude of the transient, and accounts for the low degree of saturation of the indicator dye during the recording. To estimate the properties of these two buffers, we compare the time course of fluorescence transient evoked by two broadened action potentials to the one obtained through computational modeling, both in the control condition and upon application of EGTA. Our results indicate that the fast buffer comprises about 10 to 15% of the total buffering capacity, previously estimated by Tank et al. (1995) to equal about 600 in this preparation, with the remaining 85-90% of the buffering ratio contributed by the slow buffer. We infer that the slow buffer has low affinity ($K_D^{\text{slow}} > 1 \mu\text{M}$), is present in large concentration ($B_{\text{slow}}^{\text{Total}} > 500 \mu\text{M}$), and we estimate its unbinding rate to range between 1 s^{-1} and 4 s^{-1} . Finally, we also estimate the following bounds on the affinity and total concentration of the fast ECB: $K_D^{\text{fast}} > 0.4 \mu\text{M}$ and $B_{\text{fast}}^{\text{Total}} > 20 \mu\text{M}$.

INTRODUCTION

Calcium signaling plays a crucial role in the regulation of a vast number of most vital cellular processes. The ability of calcium ions (Ca^{2+}) to exert control over a diverse set of cell mechanisms critically depends on the precise spatio-temporal regulation of its intracellular concentration. The most direct and immediate route of such regulation is provided by endogenous Ca^{2+} buffering substances, which typically bind 98 to 99.9% of Ca^{2+} ions entering the cytoplasm (cite reviews). Therefore, understanding the spatio-temporal dynamics of intracellular Ca^{2+} signaling requires the knowledge of the properties of ECBs. This is particularly true in the case of synaptic transmission. Due to a direct molecular linkage with the SNARE complex, the separation between presynaptic Ca^{2+} channels and the nearest synaptic vesicles can be as short as 20 to 50 nm (Sudhof, 2004). Given the short distance, a vesicle should be exposed to a large increase in $[\text{Ca}^{2+}]_i$ within a fraction of a millisecond after a Ca^{2+} channel opening (Neher, 1998). Furthermore, the minimal lag time between Ca^{2+} influx and the detection of postsynaptic response has been estimated to be 50 to 200 μs (Llinás et al., 1981; Sabatini and Regehr, 1996). Therefore, in order to understand the dynamics of calcium activated vesicular secretion, it is necessary to know the distribution of intracellular free Ca^{2+} at a resolution of nanometer and microsecond, in a Ca^{2+} “nanodomain” surrounding an open Ca^{2+} channel. It has not been possible to monitor $[\text{Ca}^{2+}]_i$ with such a fine spatial and temporal details. Therefore, a precise account of presynaptic Ca^{2+} dynamics within nanodomains requires inferences made from mathematical modeling of Ca^{2+} diffusion and binding to Ca^{2+} buffers. However, with the exception of chromaffin cells where the characteristics of the fixed ECB have been rigorously examined (Xu et al., 1997), in most cells the data on the concentration and the Ca^{2+} -binding properties of ECBs is not available. In many preparations, computational modeling of Ca^{2+} distribution relies on the buffering parameters estimated in chromaffin cells (Matveev et al., 2004; Tang et al., 2000). Adding to the uncertainty, the properties of mobile ECBs that are typically washed out during whole cell recording are not fully characterized (Neves et al., 2001; Roberts, 1993; Zhou and Neher, 1993). Experiments have consistently suggested the importance of mobile buffers, and attempted to resolve this problem. For example, by dialyzing reconstituted Ca^{2+} buffers back into cells and investigating the dynamics of $[\text{Ca}^{2+}]_i$, it is possible to infer the behavior of some of the Ca^{2+} buffers in vivo (Blatow et

al., 2003; Edmonds et al., 2000; Lee et al., 2000; Schmidt et al., 2003). Alternatively, properties of ECBs have been characterized in terms of EGTA or BAPTA equivalents (Neves et al., 2001; Roberts, 1993). In this report, we attempt to infer the kinetic properties of ECBs at the crayfish inhibitor by analyzing the decay of Ca^{2+} transients recorded at a high time resolution.

The neuromuscular junction of the crayfish opener has been extensively used as a model for the investigation of synaptic plasticity, due to its robust short and long term synaptic enhancement with minimal transmitter depletion (Atwood and Wojtowicz, 1986). The presynaptic axons in this preparation are accessible and allow simultaneous monitoring of presynaptic action potentials, $[\text{Ca}^{2+}]$, and transmitter release. It was one of the first presynaptic preparations where quantitative Ca^{2+} imaging studies provided an estimate of the Ca^{2+} influx evoked by individual action potentials, as well as the estimates of the endogenous buffering ratio and Ca^{2+} extrusion rate (Delaney et al., 1989; Tank et al., 1995). In order to further advance the understanding of this system, we seek to account for a gradual decay of Ca^{2+} transients within 50-100 ms after an action potential, referred to in this paper as the *early decay*. A recent analysis of early decay has shown that blockers of known extrusion and sequestration processes have no impact on the time course of Ca^{2+} concentration on this time scale (Lin et al., 2005). In addition, numerical simulations incorporating known constraints of the crayfish NMJ predict a plateau during the time window of early decay as long as ECBs with fast kinetics are assumed (*ibid.*). Adjustment of such simulation parameters as buffer affinity, mobility or terminal dimensions were not sufficient to achieve a gradual early decay of the simulated Ca^{2+} bound indicator dye. Based on these observations, it was proposed that the early decay could be due to a slow ECB. However, it was noted that a single class of slow buffer cannot account for the experimental results because it has virtually no buffering power during the brief period of action potential activated Ca^{2+} influx and would not prevent the saturation of a low affinity indicator. It was therefore proposed that the crayfish inhibitor contains both fast and slow ECBs. The former is capable of competing with fast Ca^{2+} indicators while the latter dictate early decay time course. This report focuses on defining the concentration and rate constants of a slow ECB that, together with a fast ECB, could fully account for the amplitude and time course of fluorescence transients.

METHODS

Experimental procedures

Indicator concentration

Final concentrations of the injected indicators were estimated to be 200-400 μM . The indicator concentration was estimated by visually comparing the fluorescence intensity of an injected axon and a dye-filled capillary tube of similar diameter. The capillary tube was filled with known concentrations of the dyes in the presence of 100 nM Ca^{2+} , prepared from Calcium Calibration Buffer Kit with 1 mM Mg^{2+} (Molecular Probes C-3721). With an indicator concentration of 2.5-5 mM in the injection pipette, there is typically a 1 to 10 dilution between the pipette and final intracellular concentrations. When the effect of EGTA was investigated, 20 mM EGTA was included in the injection pipette, along with 2 mM MgOrg and 400 mM K^+ Methansulphonate. The final EGTA concentration was assumed to be diluted to a similar extent as MgOrg ($\sim 10\text{X}$), i.e. $\sim 2\text{-}4$ mM.

Computational modeling of fluorescence transients

Single compartment model of buffered Ca^{2+} diffusion

The search for rate constants and concentrations of slow and fast ECBs was performed using a single-compartment model of Ca^{2+} dynamics. As was previously observed (Lin and Allana, 2005), the time course of Ca^{2+} transients recorded using low mobility, dextran-coupled indicators and near-membrane indicators was not significantly different from the time course of Ca^{2+} decay recorded with highly mobile indicators, which suggests that the spatial equilibration plays an insignificant role in shaping early decay. The effect of spatial diffusion on our results will be discussed in more detail below (See Fig. 9). The one-compartmental model gives

$$\begin{cases} \frac{dCa}{dt} = \sum_{i=1}^{N_b} \left\{ -k_i^{on} Ca (B_i^{Total} - B_i) + k_i^{off} B_i \right\} + \frac{1}{2FV} I_{Ca}(t) - k_{pump} (Ca - Ca_{bgr}) \\ \frac{dB_i}{dt} = k_i^{on} Ca (B_i^{Total} - B_i) - k_i^{off} B_i \end{cases} \quad (1, 2)$$

where Ca and B_i denote the concentrations of Ca^{2+} and the Ca^{2+} -bound i -th buffer (or dye) species, respectively, k_i^{on} and k_i^{off} are the binding and the unbinding rates of the i -th buffer, and B_i^{Total} is its total concentration. $I_{Ca}(t)$ denotes the Ca^{2+} current, F is the Faraday constant, and V is the cell volume. In the first equation, summation is extended over the number of buffers present in the cell, N_b , which includes the Ca^{2+} indicator dye, B_{ind} . k_{pump} denotes the rate of Ca^{2+} extrusion by membrane pumps, which equals $k_{pump} = (1 + \kappa_{total}) / \tau_{pump}$, where $\kappa_{total} = 600$ is the total resting buffering capacity, and $\tau_{pump} \approx 5$ sec is the estimated extrusion time (Tank et al., 1995). Equations (1) are integrated numerically using the Calc ("Calcium Calculator") modeling software running in ODE-only mode (<http://web.njit.edu/~matveev/calc.html>). Analysis of certain limiting cases allowing for exact solution of Eqs. 1-2 is given in the Appendix.

Simulated Ca^{2+} indicator dye fluorescence

Assuming that one of the buffer species represents the Ca^{2+} -sensitive indicator MgOrg, fluorescence time course is modeled as

$$F(t) = \frac{B_{ind}(t) - B_{ind}^{bgr}}{B_{ind}^{Total} - B_{ind}^{bgr}} \quad (3)$$

where $B_{ind}(t)$ is the concentration of the Ca^{2+} -bound indicator calculated by solving Eqs. 1-2, B_{ind}^{Total} is the indicator dye total concentration, and

$B_{ind}^{bgr} = [Ca^{2+}]_{rest} B_{ind}^{Total} / (K_D^{ind} + [Ca^{2+}]_{rest})$ is the resting background value of $B_{ind}(t)$. We assume a resting background Ca^{2+} concentration of $[Ca^{2+}]_{rest} = 0.1 \mu M$. Experimental fluorescence transients were recorded using a low affinity MgOrg indicator dye, with concentration estimated to lie in the range $B_{ind}^{Total} = 200-400 \mu M$. We assume its Ca^{2+} -binding rate to equal $0.5 \mu M^{-1} s^{-1}$. Its affinity, published by Molecular Probes, is $K_D^{ind} = 12 \mu M$, yielding an off rate of $k_{ind}^{off} = 6 ms^{-1}$. The fast off rate is consistent with previous report

showing MgOrg fluorescence transient in skeletal muscle to be faster than that of Magnesium Green ($K_D=7 \mu\text{M}$), and comparable to that of Magnesium Fura-2 ($K_D=42 \mu\text{M}$) (Zhao et al., 1996). The mobility of the indicator is $0.118 \mu\text{m}^2\text{s}^{-1}$.

MgOrg binds Mg^{2+} with a K_d of 3.9 mM. Although the resting Mg^{2+} concentration at the crayfish NMJ is unknown, we assume that there is no rapid change in $[\text{Mg}^{2+}]$ during the early decay. Therefore, a constant fraction of Mg^{2+} bound MgOrg contributes to background fluorescence. Since the Ca^{2+} transient in this report is quantified by calculating the action potential-activated peak MgOrg fluorescence as a fraction of the maximal fluorescence activated by a prolonged Ca^{2+} influx (Lin et al, 2005), the presence of Mg^{2+} -bound MgOrg should not introduce an error into the calculation.

MgOrg has been chosen over other indicators on the bases of its Ca^{2+} binding affinity and long excitation wavelength. Illumination of crayfish NMJ with UV, and to a less extent blue light, creates strong autofluorescence, which, depending on pigment distribution, is typically non-uniform spatially. As a result, the correction of background fluorescence is difficult with photodiode imaging. There are several long wavelength Ca^{2+} indicators, some of them, such as meg-fura-red, exhibit anomaly in fast Ca^{2+} transient (Zhao et al., 1996), while others, such as Rhod-FF, have such a low background fluorescence that it becomes impossible to gauge the concentration injected in the axon. Overall, MgOrg is bright and typically is observed against a black background, i.e. without autofluorescence.

Estimates of presynaptic Ca^{2+} influx

The early decay of Ca^{2+} transients was analyzed from experiments where broad action potentials were used, in the presence of 20 mM TEA and 1 mM 4-AP. A previous study has shown that the peak amplitude of fluorescence transient evoked by broad action potentials was about 10 times larger than that measured in physiological saline (Vyshedskiy and Lin, 2000). Since low affinity Ca^{2+} indicator (Magnesium Green $K_d = 7 \mu\text{M}$) was used in that study, it is reasonable to assume that there was minimal indicator saturation and that a broad action potential triggers a Ca^{2+} influx at least 10 times larger than that activated by a narrow action potential recorded in physiological saline. According to an estimate of Tank et al. (1995), a single action potential leads to a Ca^{2+} influx of $3\pm 2 \times 10^{-18}$ mole into the terminal. Assuming a spherical bouton of 3 μm in radius,

this corresponds to a step increase of average total (bound plus unbound) whole-terminal Ca^{2+} concentration of about $27 \pm 18 \mu\text{M}$. This value is consistent with but somewhat larger than the $15.5 \pm 10 \mu\text{M}$ range inferred from the study by Tang et al. (2000). Therefore, we assume that a broad action potential elevates the total Ca^{2+} concentration by $\Delta\text{Ca}_{\text{AP}} = 50$ to $400 \mu\text{M}$. Given the endogenous buffering capacity of 600, this corresponds to an increase in free Ca^{2+} of between 0.08 and $0.67 \mu\text{M}$.

Comparison of model and experimental fluorescence transients

For a given set of buffering parameters, simulated fluorescence time course $F_{\text{sim}}(t)$ is computed according to Eq. 3, rescaled by a constant calibration factor α , and its deviation from the experimentally measured time-course $F_{\text{exp}}(t)$ is quantified by the weighted *sum of squared residuals*:

$$SSR = \int_0^T \frac{[F_{\text{exp}}(t) - \alpha F_{\text{sim}}(t)]^2}{\sigma(t)^2} dt \quad (4)$$

Here $\sigma(t)$ denotes the standard deviation in the experimental measurement of $F_{\text{exp}}(t)$, and the integral extends over the duration of the recording (see Fig. 1). The integral is computed as a simple sum over the time sample points; the fluorescence is sampled with a 10 kHz (0.1 ms) time resolution. Because of the variance term in the denominator of the weighted SSR deviation measure, the more accurate the measurement at a particular time point, the higher is the contribution of the corresponding residual to the total deviation. This weighting ensures that minimizing SSR is equivalent to maximizing the likelihood function.

In Eq. 4, we restrict integration to the decay intervals in the fluorescence time-course only, excluding the 8 ms time intervals corresponding to the two rising phases; therefore, we do not attempt to fit the fluorescence increase during the two action potentials. This is justified since the assumption of spatial equilibrium implicit in the single-compartment approach is the least accurate during the rapid rising phases. Further, neglecting the rising phase removes the necessity to accurately reproduce the time course of Ca^{2+} influx.

The use of the scaling parameter α in equation 4 eliminates the problem of uncertainty in the calibration between the recorded fluorescence signal and the inferred

absolute value of bound dye concentration given by Eq. 3. This scaling factor is chosen in such a way that the deviation given by Eq. 4 is minimized; the extremum condition $d(SSR)/d\alpha=0$ leads to an equation

$$\alpha = \int_0^T \frac{F_{\text{exp}}(t)F_{\text{sim}}(t)}{\sigma(t)^2} dt \bigg/ \int_0^T \frac{F_{\text{sim}}^2(t)}{\sigma(t)^2} dt \quad (5)$$

Because of this scaling procedure, the deviation measure given by Eq. 4 compares only the time courses of predicted and measured fluorescence transients, and not their magnitudes. The amplitude of the transient is constrained independently by comparing the amount of dye saturation during the pulse with the experimentally determined upper bound on its value (see Eqs. 6 and 7 below).

The buffering parameters are constrained by fitting the fluorescence data recorded both in the absence and in the presence of EGTA (Figs. 1 A, B). When calculating the deviation between model and experiment using Eq. 4 for the EGTA case, we use the value of the calibration factor α that was obtained by fitting the control data, thereby assuming that the concentration of the indicator dye is the same under both experimental conditions. The reason for using only the control data when evaluating the calibration factor is that the measurement error was larger for the EGTA condition (see below).

Goodness of fit

The combined deviation measure shown in grayscale in Figs. 4 D, 6, 7 and 8 includes a sum of deviations calculated in the control condition and in the presence of EGTA, and incorporates an upper bound on the peak AP-evoked fluorescence. The EGTA data contribution to the combined deviation is weighed more lightly due to a “ringing” artifact in the recording, arising from a mechanical coupling (cf. Figs. 1 A and 1 B):

$$SSR_{\text{total}} = SSR_{\text{control}} + w SSR_{\text{EGTA}} + D_{\text{sat}} \quad (6)$$

The weight factor $w=0.0162$ equals the ratio of the SSR values of the control and EGTA data relative to the reference best-fit curves. D_{sat} implements the constraint on peak MgOrg saturation; it equals zero at low levels of MgOrg saturation (see Eq. 8 below).

We quantify the goodness of fit using the standard R^2 measure, which compares the weighted SSR value given by Eq. 6 with SST , the so-called *total sum of squared residuals*:

$$R^2 = 1 - SSR_{\text{total}} / SST_{\text{total}} = 1 - SSR_{\text{total}} / (SST_{\text{control}} + w SST_{\text{EGTA}}) \quad (7)$$

where SST_{control} and SST_{EGTA} are defined as the sum of squared residuals between the corresponding data and a time-independent constant equal to the average of this data over the relevant time interval. The value of R^2 can be interpreted as the fraction of the total variance present in the data which is captured by the model. Note that R^2 and SSR_{total} are linearly related. We consider the deviation between model and experiment to be acceptable if $R^2 \geq R^2_{\text{min}} = 97.5\%$. The corresponding parameter regions are shown in white in the parameter sweep plots of Figs. 4 D, 6, 7 and 8. This goodness of fit threshold is quite conservative, as illustrated by the simulations shown in Fig. 5, which correspond to parameter values lying just outside of the parameter range satisfying this bound on R^2 .

The contour plots of Figs. 2 A and 4 A indicate the value of SSR_{control} , the deviation between model and experiment for the control condition only, while Figs. 2 B and 4 B show the value of SSR_{EGTA} , the deviation for the EGTA data fit. The white parameter regions in these plots correspond to R^2 goodness of fit thresholds of $R^2_{\text{control}} = 98.5\%$ for the control data and $R^2_{\text{EGTA}} = 81.5\%$ for EGTA data. Each of these two error bounds represents half of the total deviation corresponding to R^2_{min} :

$$(1 - R^2_{\text{control}}) SST_{\text{control}} = w (1 - R^2_{\text{EGTA}}) SST_{\text{EGTA}} = (1 - R^2_{\text{min}}) SST_{\text{total}} / 2$$

Note once again that these R^2 constraints are quite conservative, as indicated for instance by a significant degree of temporal correlation remaining in the distribution of the residuals of the corresponding data fits (data not shown).

Constraint on peak saturation of MgOrg indicator

MgOrg fluorescence reaches $6\pm 1.4\%$ of its resting value at the peak of the broad action potential, as compared to $34\pm 11\%$ for a prolonged depolarization. Therefore, the dye saturation during an action potential cannot exceed an upper bound of $18\pm 7\%$ (see Fig. 4 C). This constraint is implemented by adding the following term to the total deviation measure given by Eq. 6:

$$D_{\text{sat}} = \lambda \left[\frac{F_{\text{AP}} - 0.11}{0.14} \right]_+^3 \quad (8)$$

where F_{AP} is the maximal fraction of bound MgOrg achieved at the peak of the simulated action potential (see Fig. 4 C), and the “+” subscript indicates that only positive values of this expression are accepted, which ensures that D_{sat} is zero below the low end of the $18\pm 7\%$ upper bound on F_{AP} . The Lagrange multiplier λ is set to the value of SSR corresponding to the minimal accepted value of R^2 , $\lambda = SSR_{\text{max}} = SST_{\text{total}} (1 - R^2_{\text{min}})$, so that the combined goodness of fit given by Eq. 7 is below R^2_{min} for values of F_{AP} violating the upper bound of 0.25. The power of 3 in the definition of D_{sat} ensures that this deviation measure decays rapidly for values of F_{AP} approaching the lower end of the $18\pm 7\%$ range, and grows supra-linearly for values of F_{AP} above the upper limit of this range.

Ca²⁺ binding properties of EGTA

When fitting the fluorescence time course recorded in the presence of EGTA, we relied on the results of (DiGregorio et al., 1999): $K_{D, \text{Ca}}^{\text{EGTA}} = 130 \text{ nM}$, $k_{\text{EGTA}}^{\text{on}} = 0.006 \mu\text{M}^{-1}\text{ms}^{-1}$

Geometry of the terminals for three dimensional modeling

Although most of our results are based on a single-compartmental model of Ca²⁺ diffusion and buffering, in Fig. 9 we present a comparison of these results with data obtained using full 3-dimensional simulations that take into account non-uniform spatial distribution of Ca²⁺ and buffer concentrations. The corresponding system is similar to the one described by Eqs. 1-2, but in addition includes a diffusion term in each of the equations. The resulting partial differential equations were integrated using the Calcium Calculator. The topography of the Ca²⁺ channel distribution is identical to those

published previously (Matveev et al., 2002; Tang et al., 2000). Specifically, Ca^{2+} channels in an active zone are assumed to be spaced 60 nm apart in a grid of 16 channels. This active zone is located at the center of a 1.6 μm by 1.6 μm plane. The terminal is assumed to have a height of 1 μm . Due to the symmetry, the simulated volume is a 0.8x0.8x1 μm cube, i.e. a quarter of a whole active zone with 4 Ca^{2+} channels located at the corner. Although a recent study has suggested a differential distributions of P- vs. non P-type Ca^{2+} channels (Allana and Lin, 2004), this factor is not incorporated because subtle differences in channel locations should have no impact on globally averaged fluorescence signals.

RESULTS

A single class of slow endogenous buffer.

We first investigated whether a single endogenous buffer species can give rise to experimentally recorded Ca^{2+} transients, measured as the concentration of Ca^{2+} -bound indicator dye (Eq. 3). The unknown parameters in our search are the on- and off-rate constants of the buffer, k_{on} and k_{off} . Given the rate constants, and thus K_{D} , the concentration of the buffer (B_{total}) is determined, since previous study has estimated a total binding ratio (approximately equal to $B_{\text{total}}/K_{\text{D}}$) of 600 in this preparation (Tank et al., 1995). The remaining parameters in a single compartment model, which are the Ca^{2+} influx, the EGTA and MgOrg rate constants and concentration, are all based on experimental estimates.

As shown in Fig. 1A, a single class of endogenous buffer is sufficient to account for the fluorescence decay recorded under control condition (in the absence of EGTA). We found that the unbinding rate of the buffer is the critical parameter, and the value of about $k_{\text{off}}=0.6 \text{ sec}^{-1}$ was optimal for obtaining a good fit in this case, as was found by Lin et al. (2005). However, Figure 1B shows that the fit to the fluorescence transient recorded in the presence of EGTA is quite poor for the chosen set of ECB parameters. This is because EGTA can compete quite efficiently with a slow ECB, and reduces the Ca^{2+} concentration more than what is reported by MgOrg. This result is analyzed more systematically in parameter sweep plots of Figure 2, by scanning over a wide range of values of the buffer's unbinding rate and affinity. The deviations between model and

experimental transients are indicated in grayscale (lighter shade indicates better fit). Note that the resting buffering ratio is kept fixed at 600, so the total buffer concentration increases along with the K_D in the vertical direction. In both the control and the EGTA cases, the goodness of fit is only weakly dependent on the buffer affinity and its total concentration, as long as $K_D > 1 \mu\text{M}$ ($B_{\text{total}} > 600 \mu\text{M}$). The reason for this lower bound is that the buffer becomes completely saturated at low values of K_D and B_{total} , leading to a significant retardation of early decay.

The different optimal k^{off} ranges in Figure 2 A and B suggest that it is impossible to fit the control and the EGTA data simultaneously: the single buffer model consistently overestimates the effect of EGTA on the Ca^{2+} transient, since EGTA can compete quite efficiently with a single slow ECB. This conclusion was verified for a range of values of total concentrations of EGTA ($[\text{EGTA}]_{\text{total}} = 2\text{-}4 \text{ mM}$) and the indicator dye ($[\text{MgOrg}]_{\text{total}} = 200\text{-}400 \mu\text{M}$), as well as Ca^{2+} influx ($\Delta\text{Ca}_{\text{AP}} = 50\text{-}400 \mu\text{M}$) (data not shown).

There is another reason why a single ECB is inadequate: due to its slow binding rate, it cannot effectively buffer incoming Ca^{2+} during an action potential. As a result, the estimated maximal Ca^{2+} bound indicator concentration is much higher than experimental estimates. Figure 1A shows about 50% saturation of the indicator dye at the peak of the Ca^{2+} pulse, significantly higher than maximal level of fluorescence intensity induced by a prolonged presynaptic depolarization, $18 \pm 7 \%$ ($n=5$) (Lin et al., 2005). In other words, unreasonably high Ca^{2+} transients would be predicted by a model that includes only slow ECBs. Therefore, a second buffer with rate constants comparable to those of MgOrg is likely to be present. We therefore attempt to model a system that includes two classes of endogenous buffer, one with fast and one with slow rate constants.

Possibility of a fast Ca^{2+} extrusion mechanism.

Lin et al. (2005) demonstrated that the early decay of the fluorescence is not influenced by blockers of the known Ca^{2+} extrusion and uptake pathways. Still, it can be argued that the characteristic decay of Ca^{2+} fluorescence is controlled not by a slow ECB, but by a Ca^{2+} clearance process insensitive to the blockers tested. However, this hypothesis is unlikely to be correct: even though well chosen extrusion parameters could undoubtedly enable the model to accurately recreate the early decay time course, it cannot explain the dramatic acceleration of decay in the presence of EGTA shown in

Fig. 1. This is because adding EGTA, by effectively buffering Ca^{2+} , would slow down the Ca^{2+} extrusion. This reasoning was verified by attempting to fit the control and EGTA fluorescence data using a single fast ECB ($K_D=5\mu\text{M}$, $k_{\text{on}}=0.5\mu\text{M}^{-1}\text{ms}^{-1}$), and a combination of two saturable Ca^{2+} clearance processes with different time constants and affinities. Despite a systematic scan of the rate constants and affinity parameters of the two extrusion processes over several orders of magnitude, we were unable to obtain a satisfactory fit of the recorded fluorescence transients under this assumption. As we expected, extrusion parameters that could accurately reproduce the early decay for the control condition consistently predicted a slower decay than that obtained by experimental recordings in EGTA. Therefore, the fluorescence data recorded in the presence of EGTA argues against a Ca^{2+} extrusion process as a source of early decay.

A combination of fast and slow endogenous buffers.

We next consider a system of two ECBs, where the first, slow buffer is largely responsible for the time course of the early decay, while the second, fast buffer is responsible for fast Ca^{2+} binding upon AP-triggered Ca^{2+} influx, preventing the saturation of the indicator dye (Lin et al., 2005). As demonstrated in Figure 3, in this case we are able to find a combination of buffering parameters yielding a good fit to experimental fluorescent transients, both in the control condition, and in the presence of EGTA. Note that in the control simulation (Fig. 3 A), the peak MgOrg saturation level is about 15%, consistent with the low level of Ca^{2+} bound dye observed experimentally. It should also be noted that probing the synapse with a pair of broad action potentials imposes a significant constraint on the freedom of choosing buffer parameters, by ruling out parameters that results in significant saturation during the second action potential (data not shown).

The suggestion of two ECBs leads to a large number of parameters to be analyzed, mainly the concentrations and rate constants for each buffer. In addition, the Ca^{2+} current (quantified by $\Delta\text{Ca}_{\text{AP}}$) should also be treated as a free parameter, given the uncertainty in its experimental estimate. In the following, we evaluate the constraints on these model parameters by systematically varying their values and calculating the goodness of fit (Eq. 6) for each set of values, as in Fig. 2. Since the critical parameter determining the time course of the Ca^{2+} transient decay is the $k_{\text{slow}}^{\text{off}}$, while the amplitude

of the transient is determined by the affinity of the fast buffer which shunts the transients, we first perform a systematic sweep across different values of k_{slow}^{off} and K_D^{fast} (Fig. 4 D). The on-rate of the fast buffer is kept fixed to a value reported in other preparations (Xu et al., 1997), so the fast buffer's off-rate constant is determined by K_D^{fast} . We next examine the remaining free parameter of the fast buffer, i.e. its concentration, given by the product of K_D^{fast} and the zero-Ca²⁺ binding ratio of the fast buffer, κ_0^{fast} . An assumed value of κ_0^{fast} will automatically set $\kappa_0^{slow} = (600 - \kappa_0^{fast})$. Since the interplay between the concentration of the fast buffer and the magnitude of Ca²⁺ influx determines the degree of MgOrg binding at the peak of the transient, the scan of κ_0^{fast} was carried out against ΔCa_{AP} . This is done by repeating the two-parameter sweep shown in Fig. 4 D for a set of different values of κ_0^{fast} and ΔCa_{AP} . The resulting four-dimensional parameter scan is presented as a matrix of K_D^{fast} vs. k_{slow}^{off} sweeps, with columns and rows corresponding to different values of κ_0^{fast} and ΔCa_{AP} , respectively (Fig. 6). This parameter sensitivity analysis effectively narrows down the ranges of κ_0^{fast} , κ_0^{slow} , K_D^{fast} and k_{slow}^{off} . However, these simulations are performed assuming K_D^{slow} of 10 μ M. In the third parameter scan (Fig. 7 A), K_D^{slow} is varied against k_{slow}^{off} ; the results of this scan establish a lower bound on K_D^{slow} , and show that the narrow range of k_{slow}^{off} deduced from Figs. 4 D and 6 remains valid for a wide range of values of K_D^{slow} . Finally, since the lower bound on K_D^{slow} arises from the saturation of the slow buffer and therefore should depend on the affinity of the fast buffer, K_D^{fast} , we analyze the goodness of fit as we vary K_D^{slow} against K_D^{fast} . In summary, our systematic analysis of the two buffer system involves studying the dependence of the goodness of fit on the following parameters: (1) the fast buffer affinity, K_D^{fast} , vs. the slow buffer's unbinding rate, k_{slow}^{off} ; (2) the relative resting buffering capacities of the fast and slow buffers, κ_0^{fast} and κ_0^{slow} , vs. the magnitude of AP-evoked Ca²⁺ influx, ΔCa_{AP} , and, finally, (3) the affinity of the slow buffer K_D^{slow} against k_{slow}^{off} and (4) K_D^{slow} against K_D^{fast} .

Range of optimal buffering parameters for a two-buffer system.

In Figure 4 we present the results of a sweep over the values of the unbinding rate of the slow buffer, $k_{\text{slow}}^{\text{off}}$, and the affinity of the fast buffer, $K_{\text{D}}^{\text{fast}}$ (cf. Fig. 2). Given the assumed resting Ca^{2+} buffering ratios of the two buffers of $\kappa_0^{\text{fast}}=60$ and $\kappa_0^{\text{slow}}=540$, yielding a total buffering strength of 600 (Tank et al., 1995), the total concentration of the fast buffer is varied along with its affinity, as in Fig. 2. The affinity of the slow buffer is set to $K_{\text{D}}^{\text{slow}}=10\mu\text{M}$.

We use three distinct measures when comparing the model and experimental traces. Figures 4 A and 4 B are similar to Figs. 2 A and 2 B, and demonstrate the parameter dependence of the total deviation between simulated and recorded transients (Eq. 4) in the control condition and in the presence of 4mM of EGTA. Figure 4 C shows in grayscale the regions of parameter space which are not consistent with the upper bound on the indicator dye saturation during the first action potential of $18\pm 7\%$ (see Eq. 8). In this respect the critical parameter is the affinity of the fast buffer, which plays a major role in reducing the saturation of the indicator dye by absorbing a significant fraction of incoming Ca^{2+} influx. Finally, in panel 4 D these three deviation measures are combined together (see Eqs. 6, 7), the white area indicating the values of parameters satisfying the lower bound on the goodness of fit between model and experiment of $R^2>97.5\%$. The parameter point marked with a diamond lies within this region and corresponds to the simulation shown in Fig. 3. In order to illustrate the sensitivity of the goodness of fit to the values of $k_{\text{slow}}^{\text{off}}$ and $K_{\text{D}}^{\text{fast}}$, in Figure 5 we present the simulation results for four different parameter choices corresponding to the points marked with triangles in Fig. 4. These four parameter points lie just outside of the most likely parameter region.

The simulated transient shown in panel 5 A (*dashed curve*) corresponds to a value of $K_{\text{D}}^{\text{fast}}$ lying above the optimal parameter region of Fig. 4 D, and exhibits a decay time course slower than that recorded experimentally. The increase of the time constant of early decay with increasing $K_{\text{D}}^{\text{fast}}$ is explained by the fact that the decay time is inversely correlated with the fast buffer's *instantaneous* Ca^{2+} binding ratio, $\kappa_{\text{fast}}(\text{Ca})$, which is an increasing function of $K_{\text{D}}^{\text{fast}}$ for any fixed value of the *resting* (zero- Ca^{2+})

buffering ratio, κ_0^{fast} (see Eqs. A7-A10 of the Appendix). Panel 5 C and D show opposite effects for points lying to the left and to the right of the optimal parameter range: the decay is too fast (too slow) for large (small) k_{slow}^{off} . Since k_{slow}^{off} characterizes the slow buffer's Ca^{2+} unbinding time, such dependence of fluorescence time course on k_{slow}^{off} is quite intuitive.

The parameter dependence of the goodness of fit of the EGTA data can also be understood through similar arguments, but the relationship is under an additional constraint since the quality of EGTA fit depends on the fit obtained in the control condition. This is because the scaling constant needed to match the amplitude of the observed and the simulated fluorescence time courses in control condition is applied to the EGTA condition. For example, when K_D^{fast} has a small value, the fluorescence signal will be very high due to the saturation of the fast buffer (Fig. 5 B). Under this condition, EGTA would reduce the peak amplitude by more than 50%. The opposite is true for Fig. 5 A where the peak fluorescence is low due to the presence of a large concentration of fast buffer. In this case introduction of EGTA would have a smaller effect on the peak fluorescence. Figures 5 C and D illustrate the interaction between EGTA and the slow buffer off-rate. Figure 5 C (D) shows that EGTA is more (less) effective in reducing the peak fluorescence when k_{slow}^{off} is slow (fast).

Dependence of data fit to fast buffer binding rate and Ca^{2+} influx per AP.

In simulations shown in Figs. 3-5, we assumed that the fast ECB has a resting binding ratio of $\kappa_0^{fast}=60$, or 10% of the total endogenous buffering capacity $\kappa_{total}=600$. As we showed above, this choice yields a good agreement between model and experiment. However, one should expect the optimal value of κ_0^{fast} to depend on the estimate of Ca^{2+} influx per action potential, as well as other buffering parameters. Figure 6 presents the results of the parameter sweep similar to the one shown in Fig. 4 D, for a set of different values of κ_0^{fast} and total Ca^{2+} influx, ΔCa_{AP} . Each panel in Fig. 6 is equivalent to that shown in Fig. 4 D, namely it incorporates the deviations for the control and the EGTA data, as well as the constraint on the indicator saturation (Eq. 8). Note however that Fig. 6 zooms in on a narrower range of K_D^{fast} and k_{slow}^{off} values, as

compared to Fig. 4. Finally, we assume that neither buffer can have a concentration above 20 mM. Given a certain binding ratio κ_0 , this translates into an upper limit on the K_D value of $(20/\kappa_0)$ mM.

Each of the four panel columns in Fig. 6 corresponds to a distinct value of κ_0^{fast} , which also determines the binding ratio of the slow buffer via $\kappa_0^{slow} = 600 - \kappa_0^{fast}$. Inspection of the abscissa ranges of the white parameter areas yielding the best fit between model and experiment shows that k_{off}^{slow} consistently resides within a narrow range 1.5-4 s⁻¹. These optimal fit areas shrink and disappear as κ_0^{fast} move outside of the 50-100 range. If κ_0^{fast} is below about 50, the fast buffer would not be able to prevent the saturation of MgOrg. Conversely, for values of κ_0^{fast} larger than about 100, the fast buffer dominates over the slow buffer in determining the time course of the Ca²⁺ transient, again leading to a reduction in the fit quality. Since we assume the total buffering ratio to equal 600, these results imply that the resting binding ratio of the slow buffer lies in the range $500 < \kappa_0^{slow} < 550$.

Inspection of the ordinate range of the optimal fit regions leads to a bound on the dissociation constant of the fast buffer: $K_D^{fast} > 0.4 \mu\text{M}$. This lower bound on K_D^{fast} follows primarily from the low saturation of the indicator (see Fig. 4 C). The low saturation condition also imposes an upper bound on total Ca²⁺ elevation per AP of about 220 μM . Finally, the combined constraints on κ_0^{fast} and K_D^{fast} lead to an estimate on the minimal total concentration of the fast buffer: $B_{fast}^{Total} > 20 \mu\text{M}$.

Lower bound on the dissociation constant of the slow endogenous buffer.

Results presented above constrain the Ca²⁺ unbinding rate and the resting binding ratio of the slow buffer, but make an arbitrary assumption on its Ca²⁺ dissociation constant, fixing it at $K_D^{slow} = 10 \mu\text{M}$. To complete the analysis of the properties of the two-buffer system, we examine the dependence of the results on the affinity of the slow buffer. To this end, in Fig. 7 A we repeat the parameter sweep similar to ones shown in Figs. 4 D and 6, this time varying K_D^{slow} along the ordinate axis, instead of K_D^{fast} . As in

the single-buffer case (Fig. 2), our results show that the value of K_D^{slow} is constrained from below by a lower bound of about 3 μM . Lower values of K_D^{slow} and B_{slow}^{Total} would predict a slower decay of the fluorescent transient than seen experimentally (Fig. 7 B, upper panel), due to the saturation of the slow buffer. Furthermore, this saturation would result in excessive accumulation of free Ca^{2+} , accentuating the effect of EGTA in reducing the peak MgOrg amplitude (Fig. 7 B, lower panel).

It is important to note that the white region in Fig. 7 A marking the most probable range of parameter values is almost parallel to the ordinate K_D^{slow} axis. This means that the constraints on the value of k_{slow}^{off} inferred from Fig. 6 is not affected by the particular value of K_D^{slow} used in our simulations, as long as K_D^{slow} and B_{slow}^{Total} are high enough to avoid saturation of the slow buffer. This agrees with the results of the qualitative analysis presented in the Appendix, which show that in certain parameter regimes, the decay rate of the Ca^{2+} transient is not sensitive to the affinity of the slow buffer (Eqs. A9 and A10).

Since the lower bound on K_D^{slow} is associated with the saturation of the slow buffer, this constraint should depend on the magnitude of the Ca^{2+} influx, ΔCa_{AP} , as well as the properties of the fast buffer which absorbs a significant portion of the Ca^{2+} transient. In particular, this minimal value of K_D^{slow} should decrease as ΔCa_{AP} is reduced. Results presented in Figure 8 agree with this argument. In contrast to the simple parameter scans of Figs. 4, 6 and 7 A, in each of the K_D^{slow} vs. K_D^{fast} scans presented in this Figure, the fit has been optimized with respect to k_{slow}^{off} at every point in parameter space. The optimal k_{slow}^{off} value for each panel remains within 1.5-4 s^{-1} range, in agreement with inferences derived from Figure 6. This procedure reduces the dimensionality of the parameter space by eliminating k_{slow}^{off} from the problem. Different panels of Figure 8 correspond to different choices of κ_0^{fast} and ΔCa_{AP} , as in Fig. 6. As we discussed above, a satisfactory data fit cannot be achieved for values of κ_0^{fast} below 50 due to the saturation of MgOrg, even though the optimal parameter area is the largest for values of κ_0^{fast} lying close to the low end of the 50-100 range that we established above. The non-trivial relationship between the optimal ranges of K_D^{slow} and K_D^{fast} can be

understood in terms of the interplay between the conditions required to accurately reproduce the Ca^{2+} transient decay time course on the one hand, and the conditions required to reproduce the effect of EGTA on the Ca^{2+} transient on the other hand (see discussion of Figs. 4, 5 and 6 above).

Figure 8 yields a lower bound on the value of K_D^{slow} of about 1 μM . Since the value of κ_0^{slow} is set to $600 - \kappa_0^{fast}$ for each given value of κ_0^{fast} , Fig. 8 allows us to infer the bound on the total concentration of the slow buffer: $B_{slow}^{Total} = K_D^{slow} (600 - \kappa_0^{fast}) > 550$ μM .

Check of reliability of the single-compartment approximation.

Finally, in Figure 9 we evaluate the accuracy of the single-compartment approximation, by comparing the simulation results shown in Figure 3 with the results obtained by integrating the three-dimensional partial differential equations describing Ca^{2+} diffusion and buffering. Note the good agreement between the two simulations, indicating that the use of a single compartment approximation is quite justified for our problem. The slight deviation between the two models is only apparent in the control (no EGTA) condition, and is most likely explained by the difference in the treatment of Ca^{2+} extrusion in the two approaches. Note also that the results of the 3D simulations were not sensitive to the assumption on the mobility of the ECBs, since the mobile Ca^{2+} indicator (as well as mobile EGTA) ensure efficient spatial re-equilibration of Ca^{2+} throughout the simulated presynaptic terminal.

DISCUSSION

Although the buffering capacities of ECBs have been estimated in many cell types (Neher, 1995), their affinities, binding rates and concentrations are inaccessible to direct measurement in crayfish NMJ, as well as most other cells. However, this information is crucial for elucidating the role of ECBs in regulating Ca^{2+} -dependent cell processes, in particular synaptic plasticity properties such as short-term facilitation (Burnashev and Rozov, 2005; Schwaller et al., 2002). In this study we have estimated the characteristics

of the fast and slow ECBs in crayfish NMJ terminals, by fitting the simulated Ca^{2+} transients to the fluorescence transients recorded using a low affinity indicator MgOrg in the presence and in the absence of EGTA. The presence of a slow ECB was inferred by Lin et al. (2005) based on the finding that neither the known Ca^{2+} extrusion mechanisms nor the diffusion of intracellular Ca^{2+} could explain the time scale of the early decay component. We have explored the parameter sensitivity of this two-buffer model, by performing an exhaustive search through the relevant parameter space, varying the model ECB properties over several orders of magnitude. The results reported here suggest that the off-rate of the slow ECB has to be within a very narrow range in order to account for the time course of early decay: $1.5 \text{ s}^{-1} < k_{\text{slow}}^{\text{off}} < 4 \text{ s}^{-1}$. Further, the experimental constraints on the maximal indicator saturation and the observed effect of EGTA on the fluorescence transients allowed us to establish bounds on the effective affinities of the two buffers ($K_D^{\text{slow}} > 1 \text{ }\mu\text{M}$, $K_D^{\text{fast}} > 0.4 \text{ }\mu\text{M}$), as well as their relative capacities and apparent concentrations ($50 < \kappa_0^{\text{fast}} < 100$, $500 < \kappa_0^{\text{slow}} < 550$, $B_{\text{Total}}^{\text{slow}} > 500 \text{ }\mu\text{M}$, $B_{\text{Total}}^{\text{fast}} > 20 \text{ }\mu\text{M}$). Thus, we infer that the two buffers have low affinity, and that the slow buffer contributes 80-90% of the total buffering capacity.

We note however that the identities and composition of the buffers remain unknown. For example, it is unclear whether the kinetic properties we inferred for the slow buffer are the sum of several independent processes with similar kinetics or a single process. The same uncertainty is also applicable to the fast buffer. Further, we assumed simple one-to-one Ca^{2+} binding stoichiometry for both buffers, which may not reflect their actual chemistry. Finally, the obtained estimates may be affected by the possible affinity of ECBs to Mg^{2+} (see below). Therefore, the constraints on total buffering capacities and concentrations inferred from our study should be viewed as constraints on the *effective*, or *apparent* values of these parameters. However, the knowledge of these apparent quantities is no less valuable, as it provides the information necessary to determine the effect of these buffers on presynaptic Ca^{2+} signals, and thereby allows to evaluate the role of ECBs in regulating exocytosis and other Ca^{2+} -dependent processes. Moreover, we note that the estimates of the slow buffer Ca^{2+} unbinding rate and the estimates of their relative capacities should be relatively insensitive to these additional considerations.

Other parameters affecting intracellular Ca²⁺ dynamics

Presynaptic terminal at the crayfish neuromuscular junction is one of the best characterized presynaptic model systems. The Ca²⁺ extrusion rate and the endogenous Ca²⁺ binding ratio have been estimated and tested with independent experimental protocols by Tank et al. (1995). In addition, the amount of Ca²⁺ influx per action potential has also been evaluated (Tang et al., 2000; Tank et al., 1995). These estimates serve as valuable constraints for the simulations in this report. Below we briefly discuss the possible sensitivity of our results to these and other parameters that were considered fixed in our work.

Total binding ratio and concentrations of injected buffers: In this study we rely on the estimate of the total Ca²⁺ binding ratio in crayfish NMJ of 600 obtained by Tank et al. (1995). It should be noted that this estimate was obtained by evaluating the decay of [Ca²⁺] on a time scale of tens of seconds to minutes, long enough for us to assume that the slow buffer proposed in this report is in equilibrium with cytosolic free Ca²⁺ and is included in the estimate. In other words, the assumption that fast and slow buffers both contribute to the total binding ratio estimated previously is justified. This value is considerably higher than those reported for most mammalian neurons and other terminals, with the exception of cerebellar Purkinje cells, cerebellar interneurons, and hair cells (Collin et al., 2005; Neher, 1995). The high binding ratio could be partly due to experimental techniques used. Specifically, sharp electrode recording and pressure injection, the only feasible approach for this preparation, do not have the uncertainty related to the wash-out of cytosolic constituents which typically occurs with whole-cell patch recordings. On the other hand, pressure injection of indicators or buffers introduces uncertainty in the estimate of dye to buffer concentration ratios. To address this issue, we repeated the exhaustive parameter scan shown in Fig. 8 with 200 μM MgOrg and with 2 mM EGTA, half the values used in all simulations above, which represent our best estimates of the concentrations of injected buffers. This reduction in the estimated concentrations of MgOrg and EGTA has a relatively minor impact on the inferred relative buffering capacities of the fast and slow buffers ($30 < \kappa_0^{fast} < 90$, $510 < \kappa_0^{slow} < 570$ vs. $50 < \kappa_0^{fast} < 100$, $500 < \kappa_0^{slow} < 550$), while the estimates of the optimal range of the slow buffer off-rate is reduced to $0.6 \text{ s}^{-1} < k_{slow}^{off} < 1.8 \text{ s}^{-1}$, and the estimate of

total AP-induced Ca^{2+} influx is reduced roughly two-fold (data not shown). Therefore, errors in the estimate of injected buffer concentrations does not change the main conclusion of this report, namely that the slow ECB should have an off-rate within a narrow range ($0.6 \text{ s}^{-1} < k_{\text{slow}}^{\text{off}} < 4 \text{ s}^{-1}$), and that the slow buffer constitutes the main portion of the overall buffering capacity.

Extrusion. The extrusion rate estimated previously is adopted without further change for two reasons. First, an extensive pharmacological screening has shown that all of the known blockers or modulators of Ca^{2+} extrusion and sequestration have no effect on the early decay (Lin et al., 2005). Therefore, the early decay is unlikely to be mediated by extrusion processes with known pharmacological properties. Second, when we examined the possibility that the early decay is due to a pharmacologically undefined extrusion process by an extensive parameter search, we found that this possibility is not compatible with the observed effect of EGTA injection on the decay of fluorescence transients recorded after EGTA injection. Therefore, since there is no experimental evidence for a fast extrusion process and the impact of this hypothetical process is incompatible with the data, no further analysis of such extrusion process is attempted.

Ca^{2+} influx: Estimates of Ca^{2+} influx per action potential from previous studies showed significant variation (Tang et al., 2000; Tank et al., 1995). We addressed this uncertainty by varying the value of $\Delta\text{Ca}_{\text{AP}}$ over an order of magnitude and showed that the range of values yielding the best fit to experimental results is well within the range estimated previously. Namely, we estimate the maximal elevation of total Ca^{2+} evoked by a single broad action potential to satisfy $\Delta\text{Ca}_{\text{AP}} < 220 \mu\text{M}$. Since we believe that a broad action potential admits a factor of 10 higher Ca influx than a physiological action potential, this upper bound agrees well with the influx estimates for physiological APs obtained by Tank et al. (1995) ($\Delta\text{Ca}_{\text{AP}} = 27 \pm 18 \mu\text{M}$) and Tang et al. (2000) ($\Delta\text{Ca}_{\text{AP}} = 15 \pm 10 \mu\text{M}$).

Ca^{2+} binding properties of the indicator dye: The remaining free parameters of this system are associated with the binding properties of MgOrg, and the on-rate of the fast buffer. The Ca^{2+} indicator used in this report, Magnesium Orange, has a reported affinity for Ca^{2+} of $12 \mu\text{M}$. It has been shown to exhibit Ca^{2+} transient faster than that recorded with Magnesium Green ($K_{\text{d,Ca}} = 7 \mu\text{M}$), and comparable to that of mag-Fura-2 ($K_{\text{d,Ca}} = 20\text{--}40 \mu\text{M}$) (Zhao et al., 1996). Therefore, the assumption of fast Ca binding rate we have adopted for this indicator is justified.

Ca²⁺ binding rates of the fast ECB and MgOrg: Although there is no direct measurement for the binding rate of the fast buffer at the crayfish NMJ, studies in excitable cells, including chromaffin cells, hair cells and neurons, all suggest the presence of fast endogenous buffers with on-rates comparable to those of fast Ca²⁺ indicators. Further, the presence of fast endogenous buffer is consistent with experimental observation that MgOrg saturation level is relatively low even with Ca²⁺ influx activated by broad action potentials. Note that none of our results are sensitive to the value of the binding rate of the fast buffer and MgOrg, which we assumed to equal 0.5 μM⁻¹ms⁻¹. This is because we are only interested in the dynamics of Ca²⁺ on the time scales of tens to hundreds of milliseconds. On these time scales, the Ca²⁺ can be assumed to be in instantaneous equilibrium with both MgOrg and the fast ECB. This was verified by repeating the simulations for a set of different values of on-rate of MgOrg and the fast ECT.

ECB affinity to Mg²⁺: As was noted above, ECB binding to Mg²⁺ may have a significant effect on our results. In fact, the low Ca²⁺ affinity of the slow ECBs may indicate a two-step Ca²⁺ binding process, whereby the binding of a Ca²⁺ ion may have to precede by the unbinding of Mg²⁺. This is true for instance for parvalbumin (PV), a slow ECB found in mammalian neurons (see below), which displays a significant affinity for Ca²⁺ (Lee et al., 2000; Schmidt et al., 2003). Assuming that the off-rate for Mg²⁺ is much faster than the off-rate for Ca²⁺, as in the case of PV, the *apparent* affinity, concentration and on-rate estimates can be translated back to their *actual* values using the relationship given by Lee et al., 2000:

$$[B_{slow}^{total}]_{actual} = [B_{slow}^{total}]_{app} / (1 + [Mg^{2+}] / K_{D,Mg}^{slow}), \quad [K_D^{slow}]_{actual} = [K_D^{slow}]_{app} / (1 + [Mg^{2+}] / K_{D,Mg}^{slow})$$

where $K_{D,Mg}^{slow}$ is the affinity of the slow buffer to Mg²⁺, and [Mg²⁺] is the intracellular concentration of Mg²⁺. Note that the estimates of the Ca²⁺ unbinding rate and of the Ca²⁺ buffering capacity range remains valid under this assumption. According to this result, the low affinity of ECBs to Ca²⁺ demonstrated in our study could be a result of large concentration of intracellular Mg²⁺ relative to $K_{D,Mg}^{slow}$.

Functional significance of slow endogenous buffers

The presence of slow ECBs has been inferred from the studies of Ca^{2+} dynamics in other cell types as well, for example in chromaffin cells (Marengo and Monck, 2000). Further, many mammalian neurons are known to express parvalbumin (PV), which is believed to exhibit slow Ca^{2+} -unbinding kinetics. With the use of reconstituted PV, in experiments on PV knock-out mice and in developmental studies of PV expression, it was shown that this protein does not significantly affect the peak $[\text{Ca}^{2+}]$ transients, but promotes a biphasic decay of $[\text{Ca}^{2+}]_i$, accelerating the fast component of $[\text{Ca}^{2+}]_i$ decay that corresponds to the time scale of early decay studied in this work, while prolonging the decay of Ca^{2+} on longer time scales (Collin et al., 2005; Lee et al., 2000; Schmidt et al., 2003). This effect of slow ECBs on Ca^{2+} was suggested to underlie its effect on short-term synaptic plasticity. Namely, it was found that the knock-out of the PV gene promotes synaptic facilitation and may turn depressing synapses into facilitating ones, presumably due to higher residual Ca^{2+} remaining after PV elimination (Caillard et al., 2000; Vreugdenhil et al., 2003). This result is quite intuitive, as the early decay time scale corresponds to the time window when synaptic facilitation is most pronounced. Interestingly, the reduction of facilitation by PV is accompanied with an increase in delayed release, presumably due to the prolonged second phase of Ca^{2+} clearance (Collin et al., 2005). This effect of PV on synaptic plasticity should be contrasted with the effect of fast ECB calbindin, which has been shown to promote facilitation by the buffer saturation mechanism (Blatow et al., 2003; Jackson and Redman, 2003; Maeda et al., 1999; Matveev et al., 2004; Neher, 1998). In cerebellar Purkinje cells, both of these buffers are expressed. In this system, the CB was shown to play a significant role in shunting the fast Ca^{2+} transients, while PV primarily accelerates the time course of the early decay of Ca^{2+} transients (Schmidt et al., 2003). Therefore, this two-buffer system is not unlike the system we have proposed, with the fast buffer capping the peak level of $[\text{Ca}^{2+}]_i$ rise and the slow buffer controlling the decay of $[\text{Ca}^{2+}]_i$ after the peak. The extrusion process then takes over and reduces $[\text{Ca}^{2+}]_i$ slowly. However, the apparent affinity of PV to Ca^{2+} is about 50 nM (Lee et al., 2000), which is a factor of 20 higher than the upper bound on the affinity of the slow ECB in the crayfish NMJ inferred in our study. This difference may in part underlie the difference between the short-term plasticity properties of Purkinje afferents and the crayfish NMJ inhibitor terminals, which exhibit

very pronounced short-term facilitation not occluded by depression. The possible relationship between the short-term plasticity properties of crayfish NMJ and the properties of ECBs inferred in this work is a subject of future investigation.

ACKNOWLEDGEMENTS

This work was supported by the National Foundation Grant DMS-0417416 to V. M. and the National Institutes of Neurological Disorders and Stroke Grant NS-31707 to J.-W. Lin

APPENDIX

Analysis of fluorescence decay time course in a fast-slow buffer system

In order to understand the dependence of the fluorescence decay time on model parameters, it is useful to consider an approximation to the model obtained from an assumption of equilibrium between Ca^{2+} and the fast buffers. Assuming a system with one slow and one fast ECB, plus a fast Ca^{2+} indicator, equations (1) reduce to (Neher and Augustine, 1992):

$$\begin{cases} \left[1 + \kappa_{fast}(Ca) + \kappa_{ind}(Ca)\right] \frac{dCa}{dt} = -k_{slow}^{on} Ca (B_{slow}^{Total} - B_{slow}) + k_{slow}^{off} B_{slow} + \frac{I_{Ca}(t)}{2FV} \\ \frac{dB_{slow}}{dt} = k_{slow}^{on} Ca (B_{slow}^{Total} - B_{slow}) - k_{slow}^{off} B_{slow} \end{cases} \quad (A1, A2)$$

where the Ca^{2+} extrusion term is neglected and the instantaneous buffering ratios are given by:

$$\kappa_{fast}(Ca) = \frac{B_{fast}^{Total} K_D^{fast}}{(Ca + K_D^{fast})^2}, \quad \kappa_{ind}(Ca) = \frac{B_{ind}^{Total} K_D^{ind}}{(Ca + K_D^{ind})^2} \quad (A3)$$

It is useful to introduce dimensionless concentration parameters $C=[Ca^{2+}]/K_D^{slow}$ and $B=[B_{slow}]/B_{Total}^{slow}$. Dividing each of the equations by $B_{Total}^{slow} k_{slow}^{off}$, we then obtain

$$\begin{cases} \frac{1 + \kappa_{fast}(C) + \kappa_{ind}(C)}{\kappa_0^{slow} \kappa_{slow}^{off}} \frac{dC}{dt} = -C(1-B) + B \\ \frac{1}{\kappa_{slow}^{off}} \frac{dB}{dt} = C(1-B) - B \end{cases} \quad (A4, A5)$$

In Eq. A4 the I_{Ca} influx term is dropped since we are only interested in the decay behavior of fluorescence rafter a brief Ca^{2+} current pulse, and do not consider its rise phase, which happens on a fast time scale. κ_0^{fast} represents the zero- Ca^{2+} binding ratio, which is close to the resting capacity of the buffer if $[Ca^{2+}]_{rest} \ll K_D$:

$$\kappa_0^{fast} = \kappa_{fast}(0) = \frac{B_{Total}^{fast}}{K_D^{fast}}; \quad \kappa_0^{slow} = \kappa_{slow}(0) = \frac{B_{Total}^{slow}}{K_D^{slow}} \quad (A6)$$

Note that equation A4 allows us to approximate the initial decay rate of Ca^{2+} transient immediately following a brief Ca^{2+} influx. Assuming for simplicity that the background Ca^{2+} concentration is negligibly low, the slow buffer is initially free: $B=0$. In this case Eq. A4 describes an exponential decay with initial decay rate of

$$r_{decay} = \frac{\kappa_{slow}^{off} \kappa_0^{slow}}{1 + \kappa_{fast}(Ca_0) + \kappa_{ind}(Ca_0)} \quad (A7)$$

Where Ca_0 is determined by the total Ca^{2+} charge entering the terminal during the action potential, ΔCa_{AP} . We assume that the Ca^{2+} concentration equilibrates instantly with the fast buffer and the MgOrg; therefore, the initial (post-AP) Ca^{2+} concentration is given by a quadratic equation

$$Ca_0 \left(1 + \frac{B_{fast}^{Total}}{K_D^{fast} + Ca_0} + \frac{B_{ind}^{Total}}{K_D^{ind} + Ca_0} \right) = Ca_{Total} \quad (A8)$$

Where $Ca_{Total} = \Delta Ca_{AP} + Ca_0$. Figure 10 compares the solution of the algebraic system (A8,A9) to a constant given by the experimental value of decay rate in control condition:

$r_{decay}^{exp} \sim 0.023 \text{ ms}^{-1}$. Notice the close correspondence between these semi-analytic results and the simulation results of Fig. 4 A. We note however, that Eqs. (A7, A8) are only an approximation, and therefore do not explain the constraints on the values of K_D^{fast} evident in Fig. 4 A.

It is useful to consider two approximations of Eqs. A7-A8, which apply respectively in the case of small and large affinities of the fast buffers.

If the concentration of free Ca^{2+} remaining upon binding to fast buffers is small (i.e. $\text{Ca}_0 \ll K_D^{\text{fast}}$, $\text{Ca}_0 \ll K_D^{\text{ind}}$), and the total capacity of fast buffers much greater than 1, equation A8 yields a well-known approximation $\text{Ca}_0 = \text{Ca}_{\text{Total}} / (\kappa_0^{\text{fast}} + \kappa_0^{\text{ind}})$. Expanding Eq. A7 to first order in Ca_0 / K_D then gives

$$r_{\text{decay}} \approx \frac{\kappa_0^{\text{slow}} k_{\text{slow}}^{\text{off}}}{\kappa_0^{\text{fast}} + \kappa_0^{\text{ind}}} \left[1 + \frac{2\text{Ca}_{\text{Total}}}{\kappa_0^{\text{fast}} + \kappa_0^{\text{ind}}} \left(\frac{\kappa_0^{\text{fast}}}{K_D^{\text{fast}}} + \frac{\kappa_0^{\text{ind}}}{K_D^{\text{ind}}} \right) \right] \quad (\text{A9})$$

Equation A9 explains the decrease of decay rate with increasing dissociation constant of the fast buffer demonstrated in Fig. 5 A.

Conversely, for large free Ca^{2+} concentration ($\text{Ca}_0 \gg K_D^{\text{fast}}$, $\text{Ca}_0 \gg K_D^{\text{ind}}$), and the total capacity of fast buffers much greater than 1, equation A8 yields $\text{Ca}_0 = \text{Ca}_{\text{Total}} - B_{\text{fast}}^{\text{Total}} - B_{\text{ind}}^{\text{Total}}$ (condition of complete saturation of fast buffers), and equation A7 is approximated by

$$r_{\text{decay}} \approx \kappa_0^{\text{slow}} k_{\text{slow}}^{\text{off}} \left[1 - \frac{K_D^{\text{fast}} B_{\text{fast}}^{\text{Total}} + K_D^{\text{ind}} B_{\text{ind}}^{\text{Total}}}{(\text{Ca}_{\text{Total}} - B_{\text{fast}}^{\text{Total}} - B_{\text{ind}}^{\text{Total}})^2} \right] \quad (\text{A10})$$

It is clear that Equation A10 also agrees with the general trend of decrease in the decay rate with increasing dissociation constant of the fast buffer, demonstrated in Figs. 4 A, 5 A, and 8. As to be expected, Eq. A10 predicts that the value of decay rate approaches $k_{\text{slow}}^{\text{off}} \kappa_0^{\text{slow}}$ as the fast buffers are getting progressively more saturated.

BIBLIOGRAPHY

- Allana, T.N., and J.W. Lin. 2004. Relative distribution of Ca²⁺ channels at the crayfish inhibitory neuromuscular junction. *J Neurophysiol* 92(3):1491-1500.
- Atwood, H.L., and J.M. Wojtowicz. 1986. Short-term and long-term plasticity and physiological differentiation of crustacean motor synapses. *Int. Rev. Neurobiol.* 28:275-362.
- Blatow, M., A. Caputi, N. Burnashev, H. Monyer, and A. Rozov. 2003. Ca²⁺ buffer saturation underlies paired pulse facilitation in calbindin-D28k-containing terminals. *Neuron* 38(1):79-88.
- Burnashev, N., and A. Rozov. 2005. Presynaptic Ca²⁺ dynamics, Ca²⁺ buffers and synaptic efficacy. *Cell Calcium* 37(5):489-495.
- Caillard, O., H. Moreno, B. Schwaller, I. Llano, M.R. Celio, and A. Marty. 2000. Role of the calcium-binding protein parvalbumin in short-term synaptic plasticity. *Proc Natl Acad Sci U S A* 97(24):13372-13377.
- Collin, T., M. Chat, M.G. Lucas, H. Moreno, P. Racay, B. Schwaller, A. Marty, and I. Llano. 2005. Developmental changes in parvalbumin regulate presynaptic Ca²⁺ signaling. *J Neurosci* 25(1):96-107.
- Delaney, K.R., R.S. Zucker, and D.W. Tank. 1989. Calcium in motor nerve terminals associated with posttetanic potentiation. *J. Neurosci.* 9(10):3558-3567.
- DiGregorio, D.A., A. Peskoff, and J.L. Vergara. 1999. Measurement of action potential-induced presynaptic calcium domains at a cultured neuromuscular junction. *J Neurosci* 19(18):7846-7859.
- Edmonds, B., R. Reyes, B. Schwaller, and W.M. Roberts. 2000. Calretinin modifies presynaptic calcium signaling in frog saccular hair cells. *Nat Neurosci* 3(8):786-790.
- Jackson, M.B., and S.J. Redman. 2003. Calcium dynamics, buffering, and buffer saturation in the boutons of dentate granule-cell axons in the hilus. *J Neurosci* 23(5):1612-1621.
- Lee, S.H., B. Schwaller, and E. Neher. 2000. Kinetics of Ca²⁺ binding to parvalbumin in bovine chromaffin cells: implications for [Ca²⁺] transients of neuronal dendrites. *J Physiol* 525 Pt 2:419-432.
- Lin, J.W., Q. Fu, and T. Allana. 2005. Probing the endogenous Ca²⁺ buffers at the presynaptic terminals of the crayfish neuromuscular junction. *J Neurophysiol* 94(1):377-386.
- Llinás, R., I.Z. Steinberg, and K. Walton. 1981. Relationship between presynaptic calcium current and postsynaptic potential in squid giant synapse. *Biophys. J.* 33:323-352.
- Maeda, H., G.C. Ellis-Davies, K. Ito, Y. Miyashita, and H. Kasai. 1999. Supralinear Ca²⁺ signaling by cooperative and mobile Ca²⁺ buffering in Purkinje neurons. *Neuron* 24(4):989-1002.
- Marengo, F.D., and J.R. Monck. 2000. Development and dissipation of Ca(2+) gradients in adrenal chromaffin cells. *Biophys J* 79(4):1800-1820.
- Matveev, V., A. Sherman, and R.S. Zucker. 2002. New and corrected simulations of synaptic facilitation. *Biophys J* 83(3):1368-1373.
- Matveev, V., R.S. Zucker, and A. Sherman. 2004. Facilitation through buffer saturation: constraints on endogenous buffering properties. *Biophys J* 86(5):2691-2709.

- Neher, E. 1995. The use of fura-2 for estimating Ca buffers and Ca fluxes. *Neuropharmacology* 34(11):1423-1442.
- Neher, E. 1998. Vesicle pools and Ca²⁺ microdomains: new tools for understanding their roles in neurotransmitter release. *Neuron* 20(3):389-399.
- Neher, E., and G.J. Augustine. 1992. Calcium gradients and buffers in bovine chromaffin cells. *J Physiol* 450:273-301.
- Neves, G., A. Gomis, and L. Lagnado. 2001. Calcium influx selects the fast mode of endocytosis in the synaptic terminal of retinal bipolar cells. *Proc Natl Acad Sci U S A* 98(26):15282-15287.
- Roberts, W.M. 1993. Spatial calcium buffering in saccular hair cells. *Nature* 363:74-76.
- Sabatini, B.L., and W.G. Regehr. 1996. Timing of neurotransmission at fast synapses in the mammalian brain. *Nature* 384:170-172.
- Schmidt, H., K.M. Stiefel, P. Racay, B. Schwaller, and J. Eilers. 2003. Mutational analysis of dendritic Ca²⁺ kinetics in rodent Purkinje cells: role of parvalbumin and calbindin D28k. *J Physiol* 551(Pt 1):13-32.
- Schwaller, B., M. Meyer, and S. Schiffmann. 2002. 'New' functions for 'old' proteins: the role of the calcium-binding proteins calbindin D-28k, calretinin and parvalbumin, in cerebellar physiology. Studies with knockout mice. *Cerebellum* 1(4):241-258.
- Sudhof, T.C. 2004. The synaptic vesicle cycle. *Annu Rev Neurosci* 27:509-547.
- Tang, Y., T. Schlumpberger, T. Kim, M. Lueker, and R. Zucker. 2000. Effects of mobile buffers on facilitation: experimental and computational studies. *Biophys J* 78:2735-2751.
- Tank, D.W., W.G. Regehr, and K.R. Delaney. 1995. A quantitative analysis of presynaptic calcium dynamics that contribute to short-term enhancement. *J. Neurosci.* 15:3539-3547.
- Vreugdenhil, M., J.G. Jefferys, M.R. Celio, and B. Schwaller. 2003. Parvalbumin-deficiency facilitates repetitive IPSCs and gamma oscillations in the hippocampus. *J Neurophysiol* 89(3):1414-1422.
- Vyshedskiy, A., and J.W. Lin. 2000. Presynaptic Ca(2+) influx at the inhibitor of the crayfish neuromuscular junction: a photometric study at a high time resolution. *J Neurophysiol* 83(1):552-562.
- Xu, T., M. Naraghi, H. Kang, and E. Neher. 1997. Kinetic studies of Ca²⁺ binding and Ca²⁺ clearance in the cytosol of adrenal chromaffin cells. *Biophys J* 73(1):532-545.
- Zhao, M., S. Hollingworth, and S.M. Baylor. 1996. Properties of tri- and tetracarboxylate Ca²⁺ indicators in frog skeletal muscle fibers. *Biophys. J.* 70:896-916.
- Zhou, Z., and E. Neher. 1993. Mobile and immobile calcium buffers in bovine adrenal chromaffin cells. *J Physiol* 469:245-273.

FIGURE CAPTIONS

Figure 1: Comparison between experimental and model fluorescence time course assuming a single endogenous buffer species with slow kinetics. Experimental fluorescence transients are shown in black, and the corresponding model fits are dashed red lines. *A*: Comparison in control condition; *B*: with 4 mM EGTA. In *A*, the amplitude of experimental trace is scaled to minimize the deviation with the model traces (Eqs. 4, 5), and the same scaling factor is then applied to traces in *B* (see Methods). Goodness of fit R^2 values are 99.0% in *A* and 46.5% in *B*. ECB parameters are $K_D=1.06 \mu\text{M}$, $B_{\text{total}}=636 \mu\text{M}$, and $k_{\text{off}}=0.64 \text{ sec}^{-1}$. MgOrg indicator dye parameters are $K_D=12 \mu\text{M}$, $[\text{MgOrg}]_{\text{total}}=400 \mu\text{M}$, and $k_{\text{off}}=6 \text{ ms}^{-1}$. In *B*, EGTA parameters are $K_D=0.13 \mu\text{M}$, $[\text{EGTA}]_{\text{total}}=4 \text{ mM}$, and $k_{\text{off}}=0.78 \text{ sec}^{-1}$ (DiGregorio et al., 1999). Total (bound + free) Ca^{2+} elevation per AP is $\Delta\text{Ca}_{\text{AP}}=200 \mu\text{M}$.

Figure 2: Goodness of fit between single-buffer model results and experimental data, as a function of buffer's unbinding rate and affinity. For each pair of values of K_D and k_{off} , the deviation between experimental and model traces is integrated over the time interval shown in Fig. 1 (Eq. 4), and the corresponding point is shaded according to the magnitude of this deviation. (*A*) Deviation between model and experiment under control condition (no EGTA). (*B*) Same, for the EGTA data. Parameter point marked by an “♦” corresponds to simulations shown in Fig. 1. Darker shades correspond to larger deviations (smaller R^2). White region in Fig. 1 *A* marks the set of parameter points yielding a goodness of fit of $R^2 \geq 98.5\%$. Gray scales are *not* equivalent in the two panels: deviations in *B* are significantly larger, given the same shade level. Note that the resting buffering ratio is kept fixed at 600, so B_{total} increases along with K_D along the vertical axis.

Figure 3: Satisfactory fit between experimental and model fluorescence time courses can be achieved in a two-buffer system. Fast buffer affinity is set to $K_D^{\text{fast}}=5 \mu\text{M}$, its

buffering ratio is $\kappa_0^{fast} = 60$, and we assume its on-rate to be comparable to that of chromaffin cells, $k_{fast}^{on} = 0.5 \mu\text{M}^{-1}\text{s}^{-1}$ (REF). Slow buffer parameters are $K_D^{slow} = 10 \mu\text{M}$, $k_{slow}^{off} = 2.5 \text{s}^{-1}$, and $\kappa_0^{slow} = 540$. Total (bound + free) Ca^{2+} elevation per AP is $\Delta\text{Ca}_{AP} = 150 \mu\text{M}$. These parameter values correspond to the point marked by a “♦” in the optimal region of the parameter space shown in Fig. 4. Total goodness of fit is $R^2 = 97.9\%$. EGTA and MgOrg indicator parameters are the same as in Fig. 1.

Figure 4. Deviation between model and experimental fluorescence time-courses in a two-buffer system, as a function of model’s buffering parameters. For each pair of values of k_{slow}^{off} and K_D^{fast} , fluorescence time-course is simulated, and the deviation between experimental and model traces is indicated in grayscale at the corresponding point in the parameter space. *A*: Control simulation (no EGTA); *B*: simulation with 4mM EGTA present. *C*: Peak saturation of the indicator dye during action potential, in control condition. Saturation above 25% violates the experimentally determined upper bound. Panel *D* combines all three deviation measures shown in *A-C* (see Eq. 6). In *A*, *B* and *D*, numbers indicate the values of the goodness of fit (R^2). In *D*, white area corresponds to the total goodness of fit of $R^2 \geq 97.5\%$, and represents the region of most likely parameter values. Parameter point marked by a “♦” corresponds to the simulation shown in Fig. 3, while the parameter points marked with triangles correspond to simulations shown in Fig. 5. All other parameters same as in Fig. 3 ($\kappa_0^{fast} = 60$, $K_D^{slow} = 10 \mu\text{M}$, $\Delta\text{Ca}_{AP} = 150 \mu\text{M}$).

Figure 5. Comparison between model and experimental fluorescence transient time courses, for parameter points marked by triangles in Figure 4. The values of k_{slow}^{off} and K_D^{fast} are: (A) 2.5s^{-1} and $30 \mu\text{M}$ (B); 0.8s^{-1} and $0.5 \mu\text{M}$; (C) 1.5s^{-1} and $5 \mu\text{M}$; (D) 4s^{-1} and $5 \mu\text{M}$. In *A*, good fit is obtained in the presence of EGTA, but not in the control condition. The opposite is true for *B*. In *A* and *C*, the decay of model fluorescence in control condition is too slow, and is too fast in *D*. In *B*, the simulated peak saturation of indicator dye is about 30%, violating the upper bound of $18 \pm 7\%$ (see text). Total goodness of fit (R^2) values for panels *A-D* are 95.8%, 90.0%, 93.3% and 93.5%,

respectively. In all simulations the resting buffering capacity of the fast buffer is kept fixed at 60, and all other parameters are the same as in Fig. 3.

Figure 6. Dependence of the deviation between model and experiment on the values of the fast buffer's capacity, κ_0^{fast} , and the Ca^{2+} influx per action potential, ΔCa_{AP} . The optimal range of parameter values is shown in white on each of the nine panels, and correspond to a goodness of fit of $R^2 \geq 97.5\%$, as in Fig. 4 D. Each of four columns corresponds to a distinct value of κ_0^{fast} , labeled at the top. Each of the three rows corresponds to a different value of Ca^{2+} influx per AP, as indicated on the right margin. The panel in the 2nd row of the 2nd column corresponds to Fig. 4 D ($\kappa_{fast}=60$, $\Delta Ca_{AP}=150$ μM). All other parameters are the same as in Fig. 4.

Figure 7. Deviation between experiment and the two-buffer model as a function of slow buffer's affinity and unbinding rate. Panel A shows combined time averaged deviation measure similar to the one shown in Figs. 4 D and 6 is plotted as a function of k_{slow}^{off} and K_D^{slow} . Goodness of fit grayscale is the same as in Figs. 4 D and 6. Diamond marks the same parameter point as in Figs. 4 and 6, and corresponds to the simulation shown in Fig. 3. Panel B present the simulated fluorescence corresponding to the parameter point labeled with a circle in A ($K_D^{slow}=0.5$ μM , $k_{slow}^{off}=2.5$ s^{-1}). Note the lower bound on the value of K_D^{slow} , and the small correlation between the optimal k_{slow}^{off} estimate and the magnitude of K_D^{slow} . Affinity of the fast buffer is kept fixed at $K_D^{fast}=5$ μM . All other parameters same as in Figs. 3-5.

Figure 8. Optimal affinity ranges of the fast and slow ECBs. Each of the two columns corresponds to a distinct value of κ_0^{fast} , labeled at the top. Each of the three rows correspond to a different value of Ca^{2+} influx per AP, as indicated on the right margin. In each of the panels, the combined deviation measure (Eq. 6) is minimized with respect to k_{slow}^{off} for every pair of values of K_D^{fast} and K_D^{slow} , and the resulting goodness of fit level is indicated in grayscale. White areas correspond to $R^2 \geq 97.5\%$, as in Figs. 4D, 6, and 7 A.

Triangles and the diamond mark the same parameter points as in Figs. 4 and 6, and correspond to simulations shown in Figs. 3 and 5. Open circle corresponds to the simulation shown in Fig. 7 B.

Figure 9. Comparison of the single-compartment model results (*solid curves*) with the results of a full three-dimensional simulation of Ca^{2+} diffusion and buffering (*dashed curves*). Simulation parameters are the same as in Fig. 3. 3D simulations were performed using the *Calcium Calculator*, with the geometry parameters of Tang et al. (2000) and Matveev et al. (2002).

Figure 10. Deviation between the value of decay rate obtained by solving the algebraic system (A7, A8) and the experimental value of decay equal to $r_{\text{decay}} \sim 0.023 \text{ ms}^{-1}$. Notice the qualitative agreement with results of model simulations shown in Fig. 4 A. Grey scale indicates the logarithm of deviation; darker shades correspond to larger deviations. The border of the white region corresponds to a deviation of $3 \cdot 10^{-3}$. Decay rate is faster than the experimental value in the bottom right parameter region, and is slower than the experimental value in the top left region. Parameter values are the same as in Fig. 4.

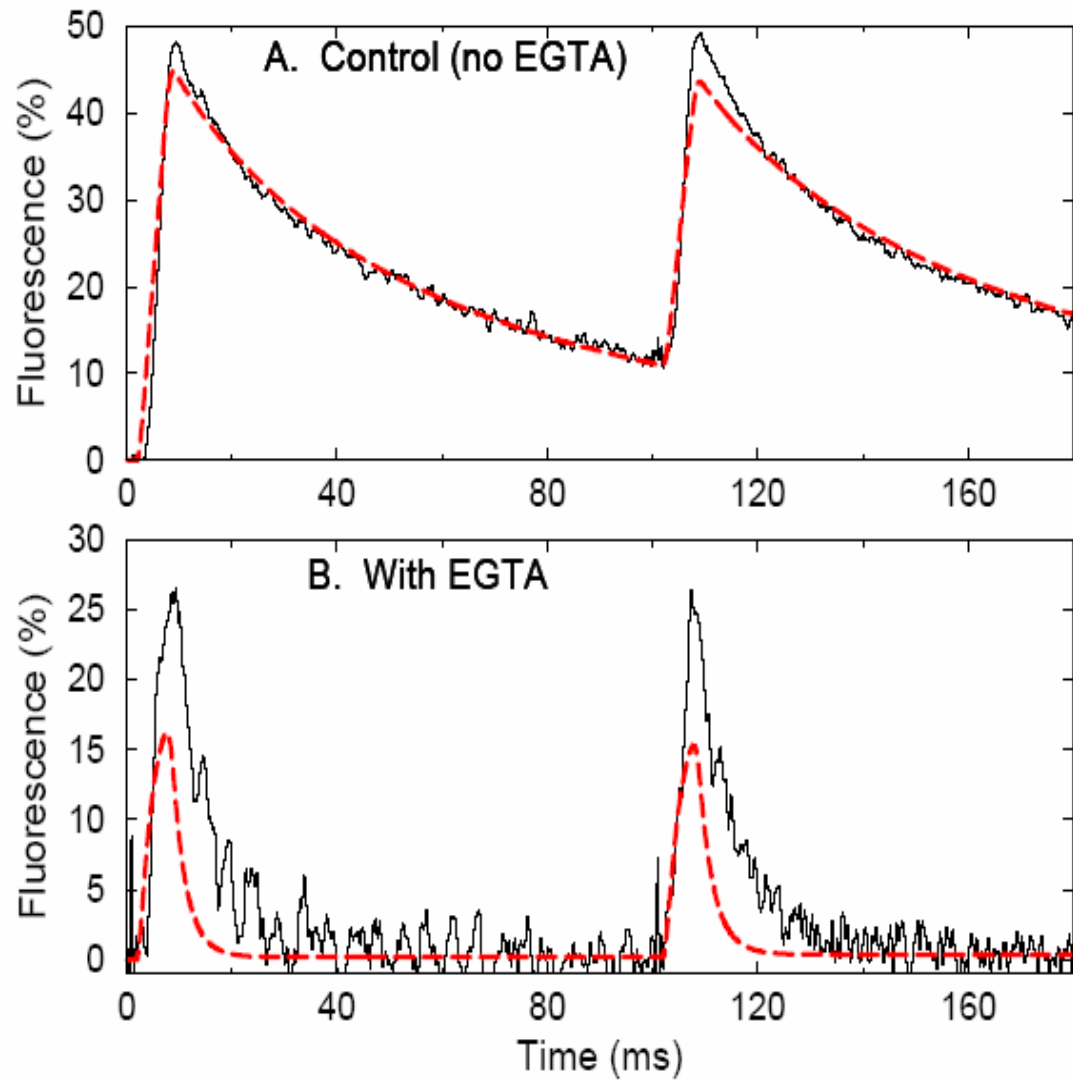


Figure 1

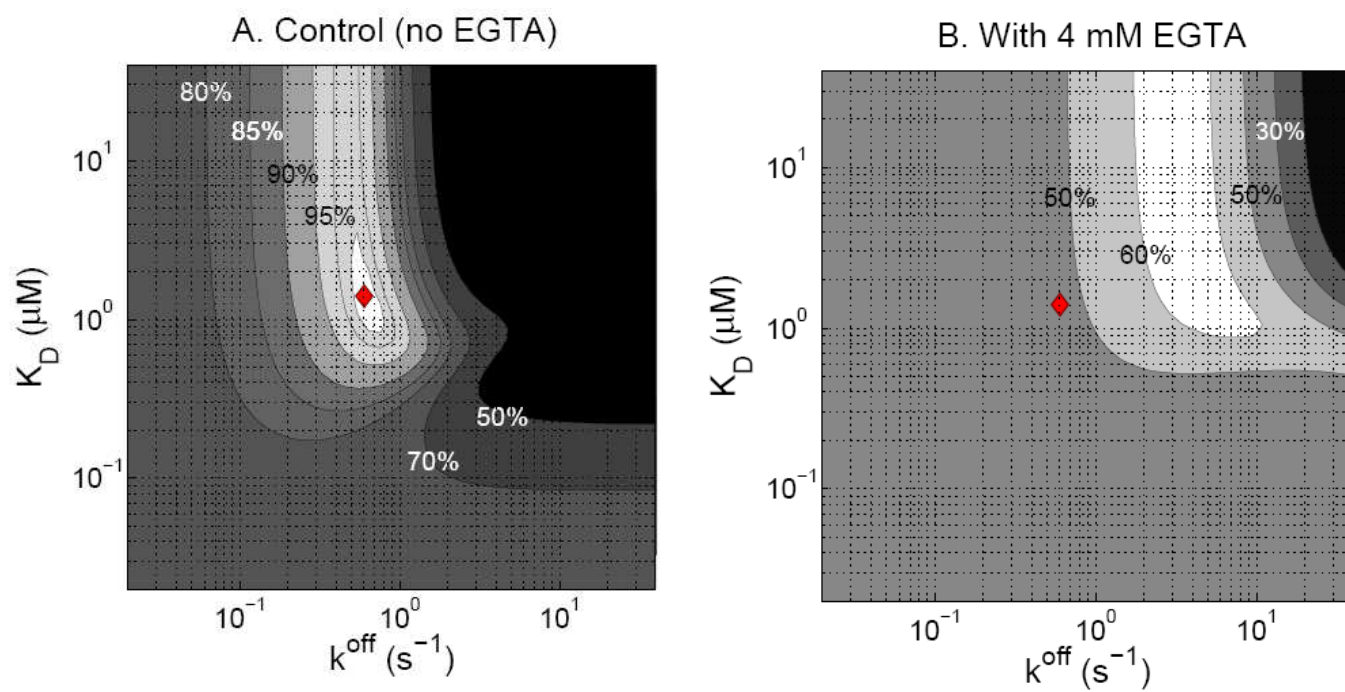


Figure 2.

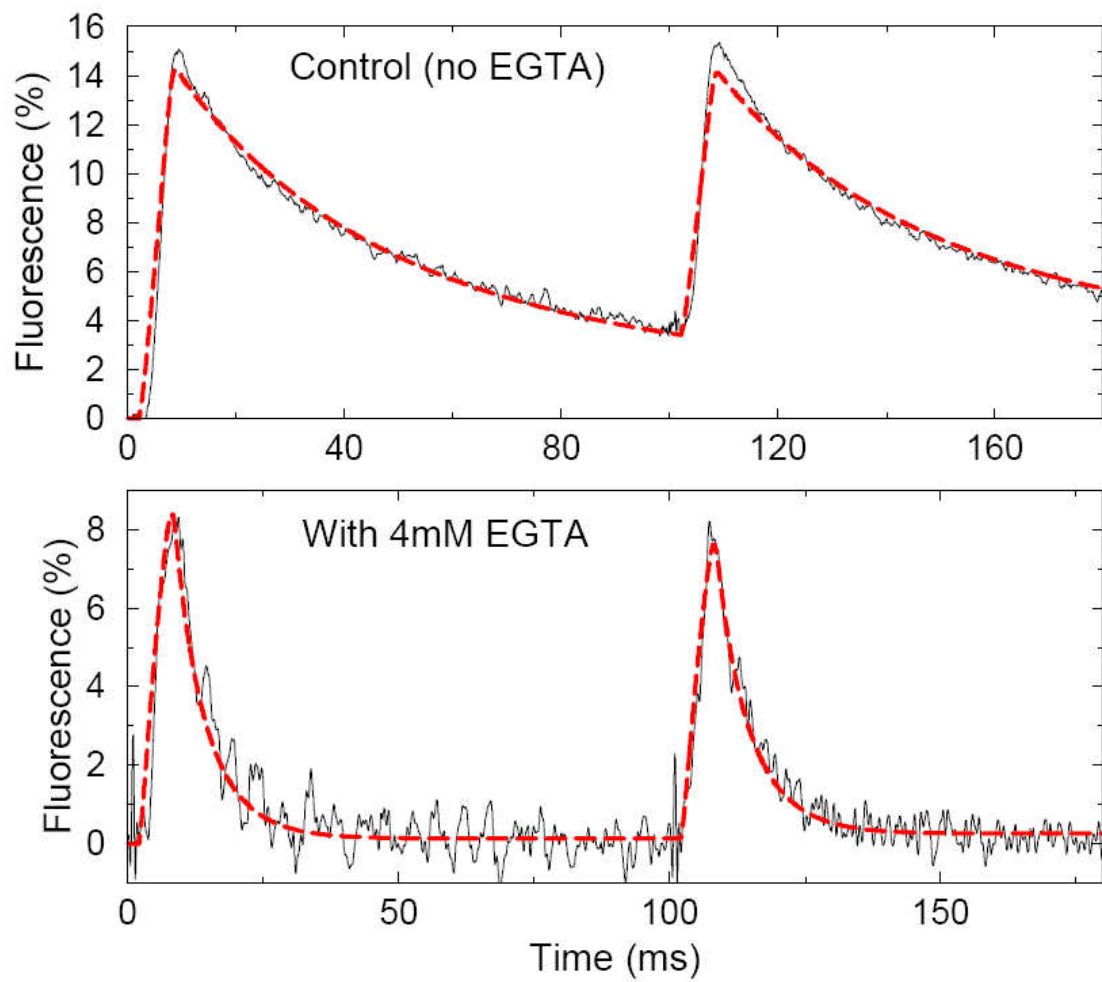


Figure 3.

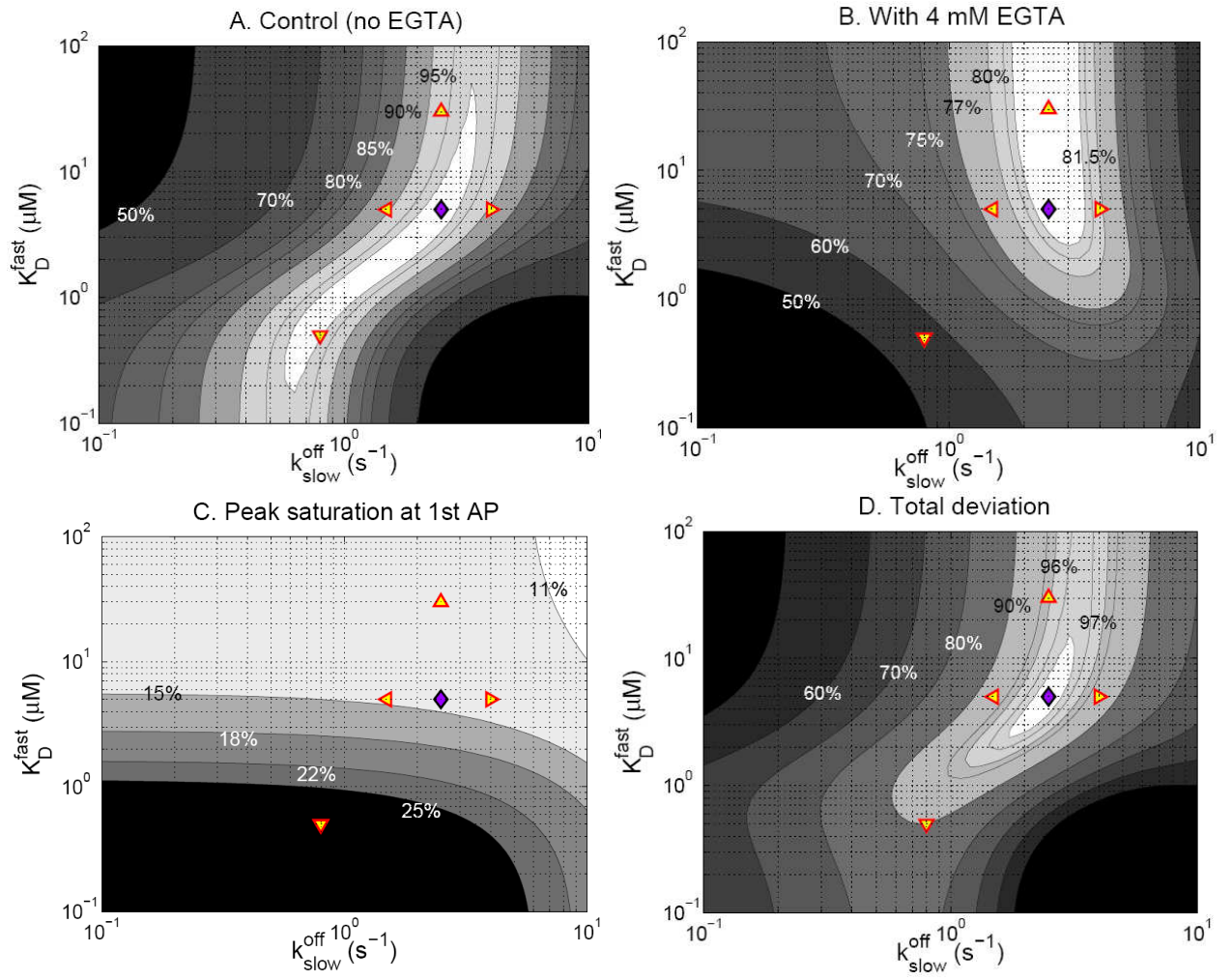


Figure 4.

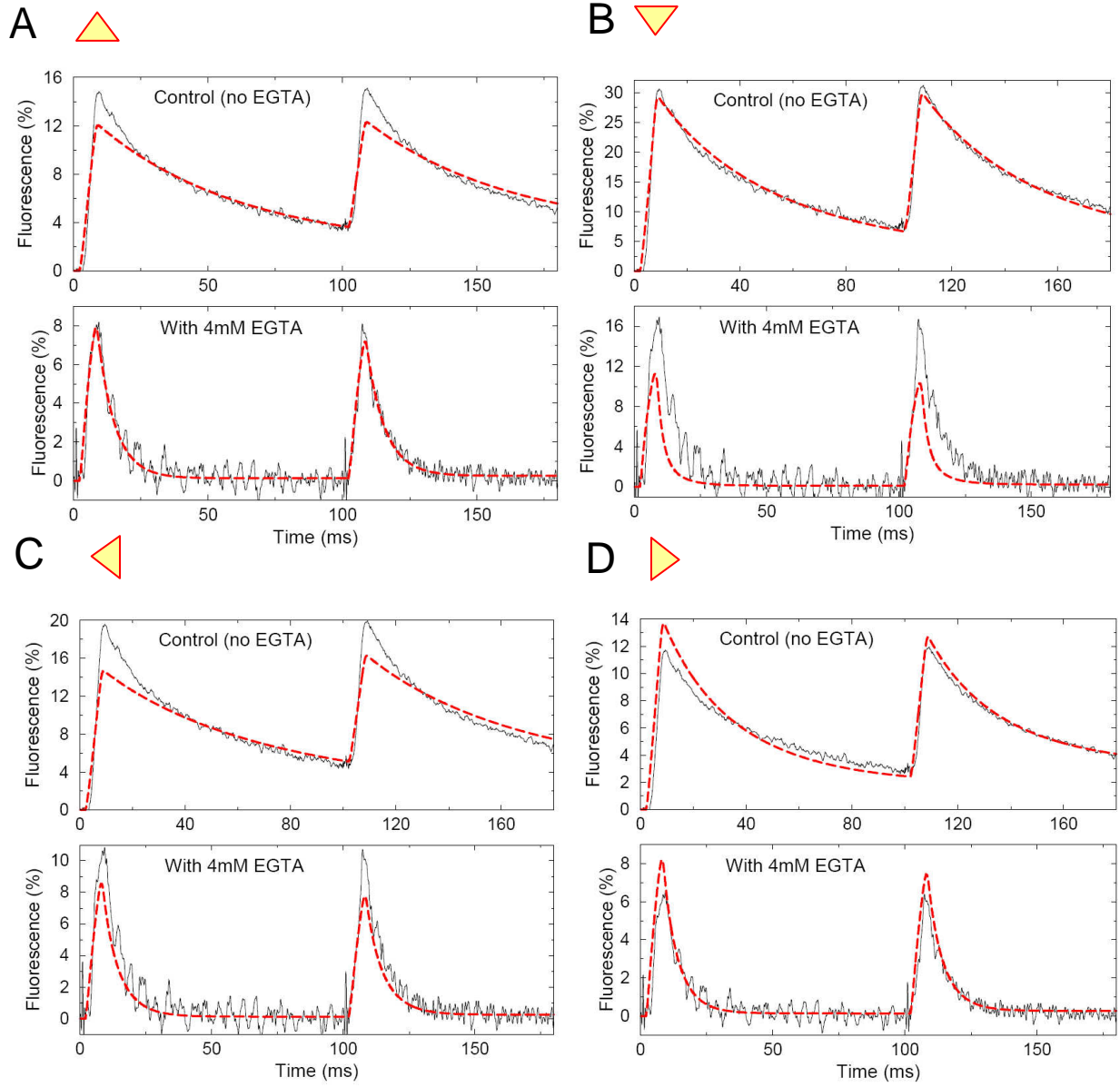


Figure 5.

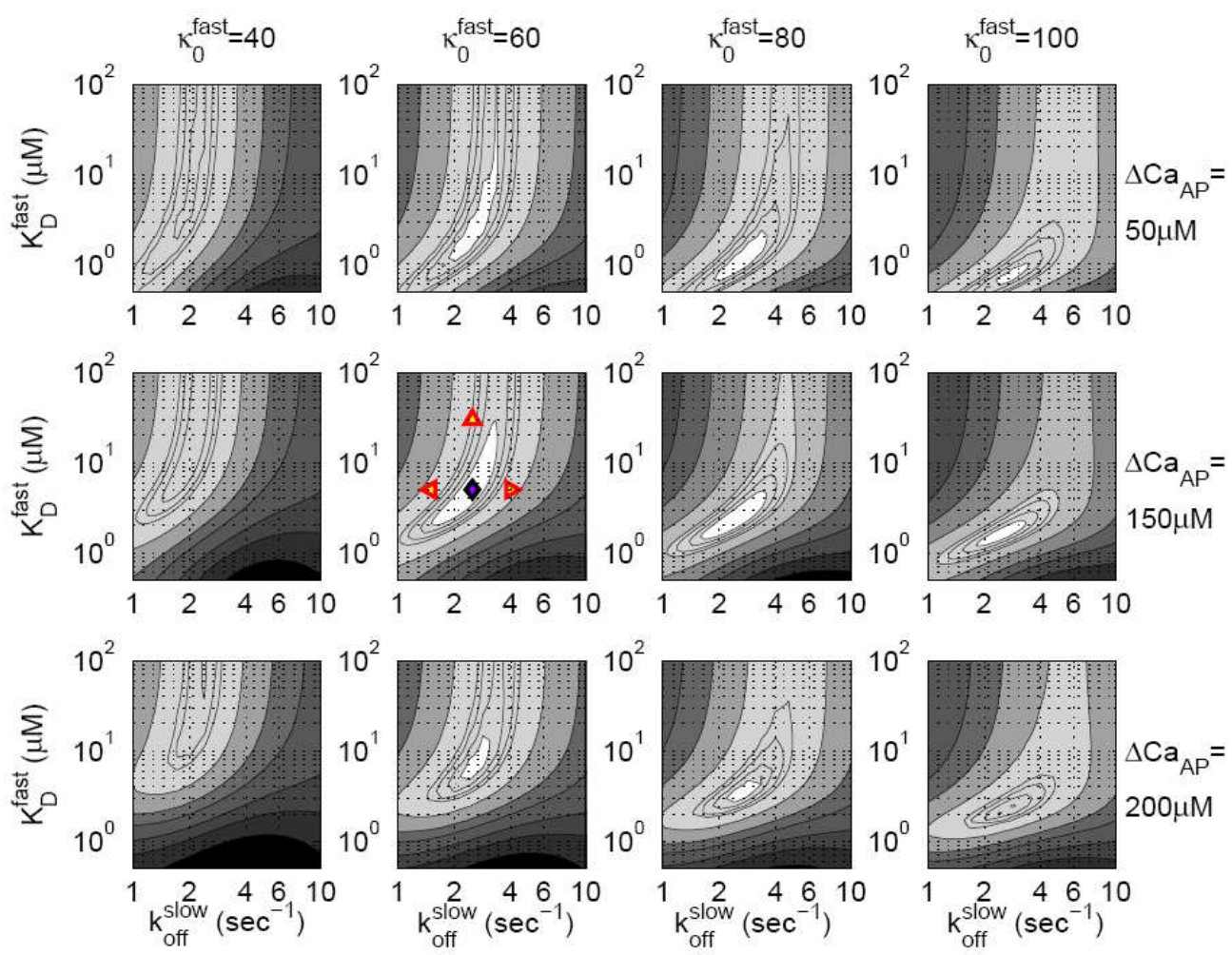


Figure 6.

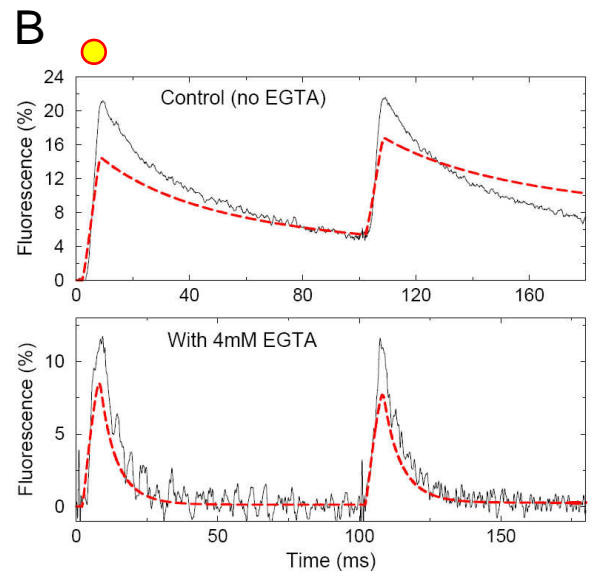
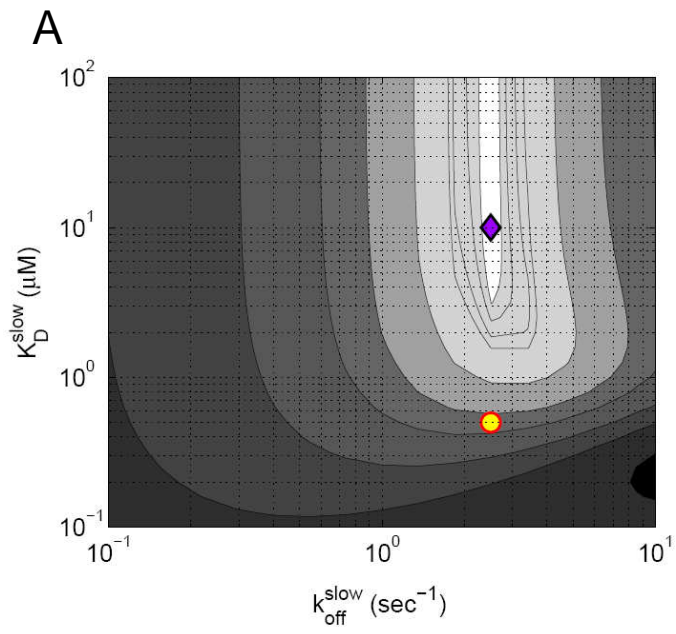


Figure 7.

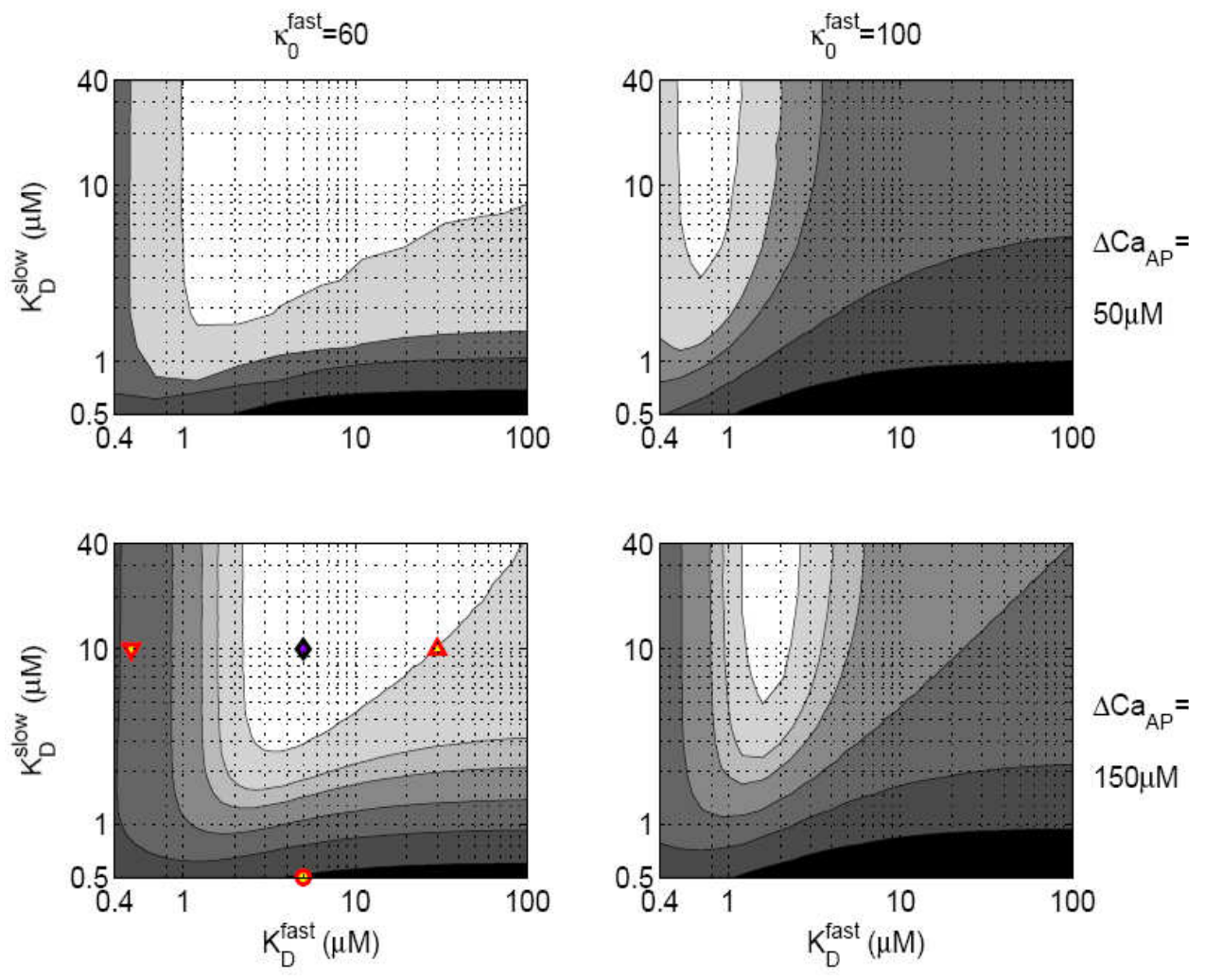


Figure 8.

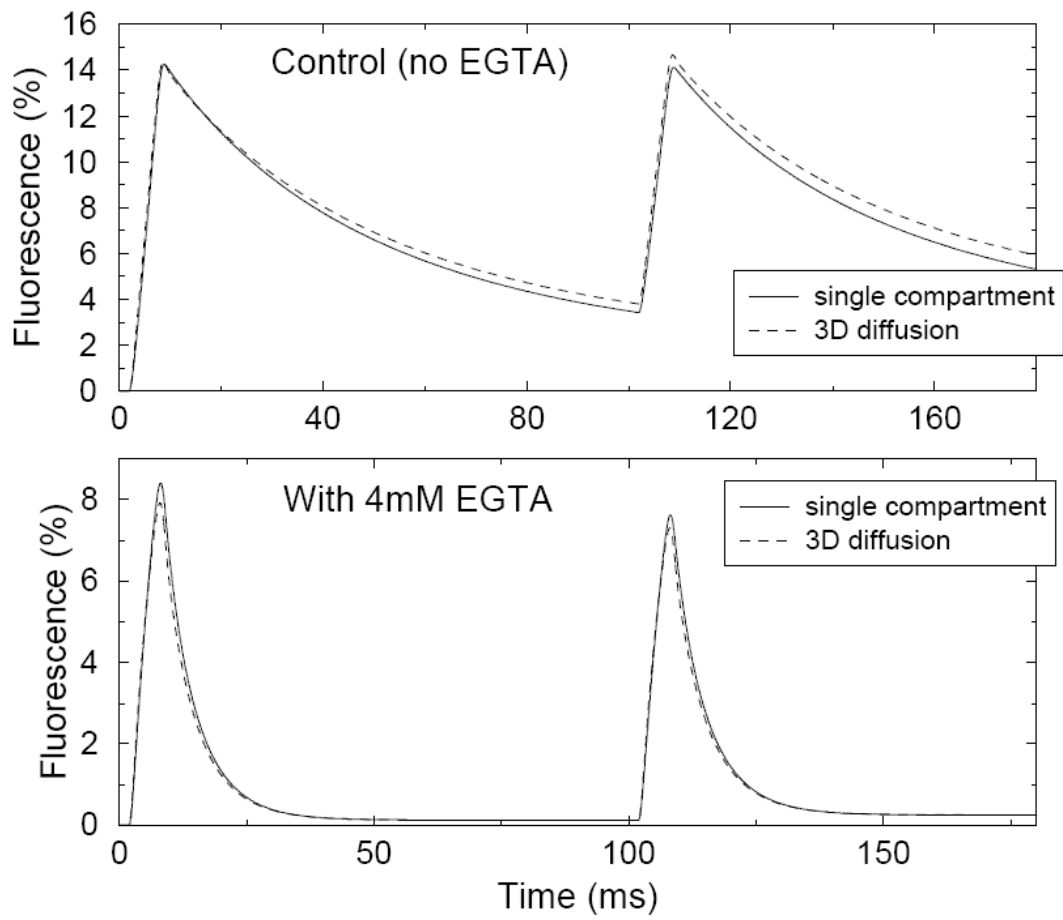


Figure 9.

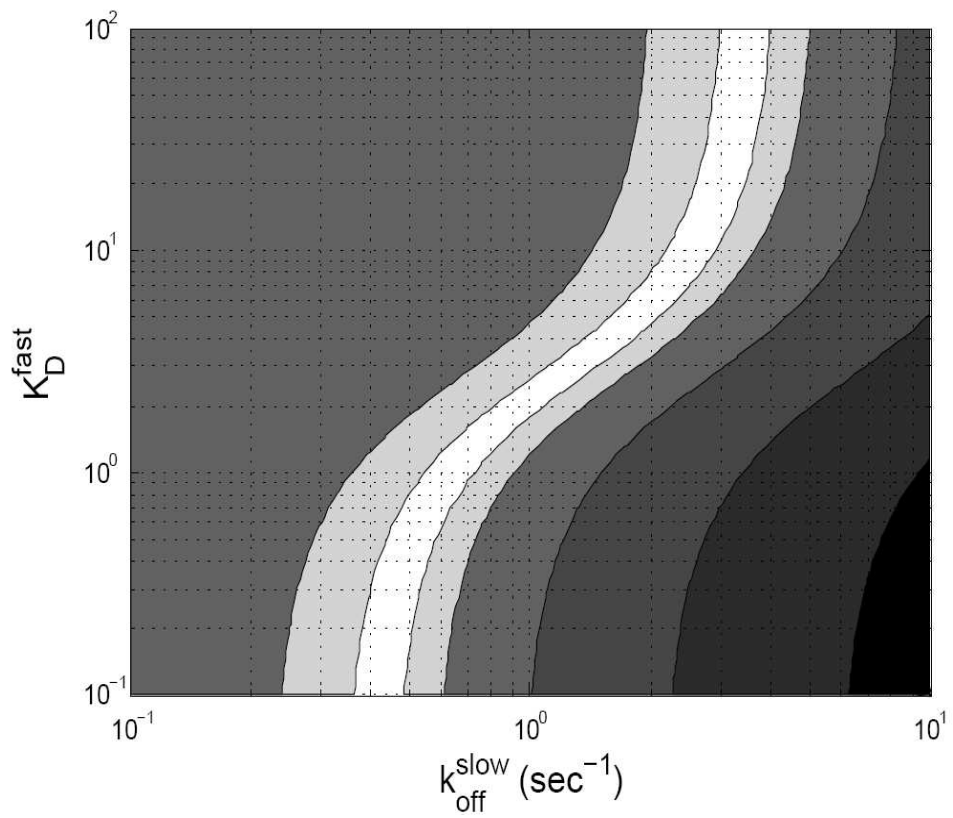


Figure 10.